A D Jefferson*[1], I C Mihai[1], R Tenchev[2], W F Alnaas[1], G Cole[2], P Lyons[2]

A plastic-damage-contact constitutive model for concrete with smoothed evolution functions

1. Cardiff University, School of Engineering, Queen's Buildings, The Parade CF24 3AA, UK. www.cardiff.ac.uk.
2. LUSAS, Forge House, High Street, Kingston Upon Thames, KT1 1HN. www.lusas.com (Paul.Lyons@LUSAS.com)

* Corresponding author. E-mail address: JeffersonAD@cf.ac.uk
Tel: +44 (0) 2920 875697

ABSTRACT

A new 3D finite element concrete model is described. The model brings together two recently developed sub-models for simulating cracking and crack contact behaviour, both of which use smoothed evolution functions, with a triaxial plasticity model component. A number of examples are presented that validate the model using a range of plain and reinforced concrete test data. These examples demonstrate that the model is numerically robust, has good equilibrium convergence performance and is objective with respect to mesh grading and increment size. The examples also illustrate the model's ability to predict peak loads, failure modes and post-peak responses.

1. INTRODUCTION

The complex nature of the mechanical behaviour of concrete has provided numerical researchers with a set of problems that nearly fifty years of work has yet to fully resolve. The multi-scale nature of this particulate material and the many mechanical mechanisms that govern its behaviour combine to make the development of a comprehensive finite element concrete model a truly challenging undertaking. Inherent flaws in early concrete models [1] became apparent in the mid 1980s as the fundamental importance of scale effects and the need for fracture mechanics concepts came to be understood [2-3]. From the finite element view point, this work demonstrated that it was not possible to use a constitutive model for softening behaviour governed by a unique stress–strain function whilst also maintaining objectivity with respect to mesh grading. Thus, it was recognised that the constitutive and computational aspects of a solution have to be considered together.

We use the word *constitutive* to describe the stress-strain behaviour of a representative volume of material with the characteristic dimension of the fracture process zone (FPZ) width. The term *computational* encompasses numerical aspects of behaviour associated with the spatial and temporal discretisations. Thus, if the predicted behaviour changes with the density of a finite element mesh, we would describe this as a computational issue. It is recognised that the underlying micro- and nano- structure of a particular material has been (and should be) used in the development of computational techniques, which implies that there should not be such a clear distinction between

what we describe as *constitutive* and *computational* aspects of modelling. Whilst this is true, we have – for convenience – continued to use these terms in our descriptions of previous numerical models.

Bazant and Oh's Crack Band model [3] was the first to address the issue of mesh dependency. Since the publication of their work, there has been a number of important computational developments that have combined constitutive and computational aspects of the modelling of concrete. These have included integral and gradient non-local models [4-12], visco regularisation schemes [13, 14], the extended finite element approach (X-FEM) [15-17], multi-scale models [18, 19] elements with embedded strong discontinuities [20-25] and elements with other enhanced interpolations to overcome problems with mesh bias [26]. Most frequently, these methods have been implemented with damage models [27,28], plasticity models [29, 30] or plastic-damage models [31]. These references represent only a small fraction of the research undertaken on modelling of concrete structures but in spite of the considerable progress made on this topic, not all of the computational problems have been fully resolved.

Whatever the combined constitutive-computational procedure adopted, the resulting non-linear systems of equations are most-frequently solved using Newton-based incremental-iterative schemes [32,33]. The authors' experience with many of the above computational techniques (i.e. viscous regularisation, integral and gradient non-local schemes and procedures which model strong discontinuities) is that situations can arise in which there is breakdown of the incremental-iterative scheme, such that equilibrium convergence cannot be achieved to an acceptable tolerance. This is true for standard Newton and modified Newton methods, solutions with automatic step selection, line-search solutions as well as solutions with various types of arc-length control [32,33].

In an attempt to avoid such difficulties, a number of researchers have developed solution procedures that either avoid (or limit) the use of iterations. These methods include the 'implicit-explicit' approach of Oliver et al. [34, 35] in which a projected state variable (e.g. a damage parameter) is used to determine a predicted consistent tangent matrix that is exact for the current increment but for which a correction is made in the subsequent stress-recovery phase. An alternative approach, based on sequential linear solutions, was proposed by Rots et al. [36]. This method was subsequently extended by Graça-e-Costa et al. [37] such that the algorithm can capture responses from non-linear materials governed by both loading and unloading behaviour of a softening material. It has also been recently applied with a new smooth crack propagation algorithm [38].

Although there are considerable benefits to using these non-iterative approaches, they can result in non-smooth responses, and would require further development before being able to cope well with constitutive models that include non-linear crack closure in combined shear and normal modes. Currently they are not naturally compatible with non-linear plasticity models for other materials, which would be an issue for solving soil-structure problems.

Crack opening and closing behaviour is important in most concrete structures, and even when the global loading is essentially monotonic in nature, some cracks open and then close again as other cracks grow [39]. Cracks in concrete are rough in nature and contact can be regained with increasing shear displacement even when a crack has a significant opening. This shear contact, often referred to as 'aggregate interlock', is important because it can be a significant load carrying mechanism in reinforced concrete structural members [40]. Crack opening and closing under normal displacements and aggregate interlock are both aspects of crack contact behaviour that should, in the

authors' opinion, be treated in a unified manner. The introduction of crack contact into a finite element concrete model can result in loss of numerical robustness because the abrupt change of stiffness that occurs upon crack closure can result in the failure of the incremental-iterative solution procedure. A fuller review of previous experimental and numerical work on modelling crack opening-closing behaviour is provided in reference [41].

The philosophy that underlies both of the sub-models described in this paper is that the convergence of a Newton type solution to a set of non-linear equations is generally more reliable when the equations are smooth and the tangent matrix is positive-definite than when the equations are discontinuous and/or the tangent matrix is non-positive-definite. The processes involved with concrete cracking and crack closure may appear to be naturally discontinuous and not readily amenable to smoothing; however, a close examination of the experimental response of concrete elements [42] suggests that these processes are not truly abrupt. This means that there is scope for using smoothed crack evolution and crack contact functions. This thinking led to two separate developments. The first of these was a new model that employs smooth crack contact and contact evolution functions to simulate rough crack contact behaviour in concrete [41]. The authors showed how this approach could be applied in an anisotropic damage model using embedded crack planes. The computational benefits of smoothing crack closure paths has also been demonstrated by Sellier et al. [43]. The second development [44] was a new approach to the simulation of damage evolution using a smoothed unloading-reloading response function within an algorithm that always uses a positive definite stiffness matrix. This approach was applied with an isotropic damage model and was shown to give considerable benefits in terms of the efficiency of the incremental iterative solution process.

The work described in the present paper brings together the two developments described in references [41] and [44], along with a plasticity model component [45-46], to form a new comprehensive 3D plastic-damage-contact model for concrete. There was considerable new work involved in making the two approaches compatible with one another and with the triaxial plasticity component, as well as with the development of a robust consistent solution algorithm for the new combined smoothed plastic-damage-contact model.

Many previous papers have described the analysis of plain concrete fracture specimens, but it is rare to find descriptions of the analysis of reinforced concrete (RC) members that include mesh convergence studies, consideration of both pre- and post-peak responses and an examination of failure modes. Although models have long since been able to obtain a reasonable pre-peak response (with some model calibration), the ability of models to simulate all of the preceding facets of behaviour is unclear. The authors' experience is that the multiple local instabilities that occur in the analysis of RC members commonly make it difficult to obtain reliable, comprehensive and accurate simulations for RC members, particularly if dominant shear cracks occur. The examples presented in this paper address all of these issues and provide a thorough examination of the performance of the model with respect to the analysis of both plain and reinforced concrete structural elements.

The paper is arranged as follows:

- Section 2 presents the essential theory of the smooth unload-reloading (SUR) and smooth contact approaches in relation to a crack-plane model and then shows how the two approaches can be brought together in a single model;

- Section 3 explains how the crack-plane model is implemented in an embedded 3D constitutive model and coupled to a plasticity model component;
- Section 4 gives guidance on material parameters;
- Section 5 gives a number of example finite element analyses, including a new mesh convergence study, and an assessment of the numerical results with respect to experimental data;
- Section 6 presents conclusions from the work.

2. CRACK-PLANE MODEL THEORY

2.1 Preliminaries

The proposed approach to modelling cracking and smooth contact is developed in terms of a crack-plane sub-model which is subsequently applied to an embedded (or smeared) crack model within finite elements. A crack-plane is defined as the mid surface of a band of material of depth h containing a crack (or micro-cracks). This band of material is associated with a fracture process zone (FPZ) [3] and thus h is interpreted as the physical width of that zone.

The orientation of the plane is defined by axes $\mathbf{r}_i$ (i=1 to 3), with unit vector $\mathbf{r}_1$ being the normal to the crack plane and $\mathbf{r}_2$ and $\mathbf{r}_3$ being orthogonal in-plane unit vectors. The crack-plane stress vector ($\tilde{\boldsymbol{\sigma}}$) and local strain vector ($\tilde{\boldsymbol{\varepsilon}}$) are as follows:

$$\tilde{\boldsymbol{\sigma}} = \begin{bmatrix} \tilde{\sigma}_{11} & \tilde{\sigma}_{12} & \tilde{\sigma}_{13} \end{bmatrix}^{\mathrm{T}} \text{ and } \tilde{\boldsymbol{\varepsilon}} = \begin{bmatrix} \tilde{\varepsilon}_{11} & \tilde{\varepsilon}_{12} & \tilde{\varepsilon}_{13} \end{bmatrix}^{\mathrm{T}} \tag{1}$$

The local strains are assumed equal to the relative displacements across the crack-band divided by the crack band width. Only the stress and strain components which can be non-zero, with the present assumptions, are included in the vectors.

The elastic crack-plane constitutive relationship is given by:

$$\tilde{\boldsymbol{\sigma}} = \tilde{\mathbf{D}}\,\tilde{\boldsymbol{\varepsilon}}_{\mathrm{e}} = \tilde{\mathbf{D}}\,\left(\tilde{\boldsymbol{\varepsilon}} - \breve{\boldsymbol{\varepsilon}}\right) \tag{2}$$

in which $\tilde{\boldsymbol{\varepsilon}}_{\mathrm{e}}$ is the elastic crack-band strain vector, $\breve{\boldsymbol{\varepsilon}}$ is the inelastic or 'fracture' strain vector and $\tilde{\mathbf{D}} = \begin{bmatrix} \tilde{\mathrm{E}} & 0 & 0 \\ 0 & \tilde{\mathrm{G}} & 0 \\ 0 & 0 & \tilde{\mathrm{G}} \end{bmatrix}$,

where $\tilde{\mathrm{E}}$ and $\tilde{\mathrm{G}}$ are the effective normal and shear elastic moduli of the crack-band material respectively.

The Cartesian stress and strain tensors are expressed in vector forms respectively as follows:

$\boldsymbol{\sigma} = \begin{bmatrix} \sigma_{11} & \sigma_{22} & \sigma_{33} & \sigma_{12} & \sigma_{13} & \sigma_{23} \end{bmatrix}^{\mathrm{T}}$ and $\boldsymbol{\varepsilon} = \begin{bmatrix} \varepsilon_{11} & \varepsilon_{22} & \varepsilon_{33} & 2\varepsilon_{12} & 2\varepsilon_{13} & 2\varepsilon_{23} \end{bmatrix}^{\mathrm{T}}$ with the fourth order elastic constitutive tensor being represented as the 6x6 Matrix $\mathbf{D}_{\mathrm{e}}$, noting that Matrix notation is used throughout this paper.

Hereafter, the terms 'stress' and 'strain' imply stress vector and strain vector respectively , unless applied to a scalar quantity.

2.2 Standard and SUR crack-plane damage model

The proposed approach may be classified as 'smeared crack model' in which cracks are represented by directional damage and where the elastic moduli associated with a particular crack-plane are degraded according to a directional damage parameter. The current work builds upon a standard crack-plane damage model, which has the following constitutive standard relationship;

$$\tilde{\boldsymbol{\sigma}} = \left(1 - \omega(\zeta)\right)\tilde{\mathbf{D}}\,\tilde{\boldsymbol{\varepsilon}} \tag{3}$$

in which the damage parameter (ω) is dependent upon the damage evolution parameter (ζ) . The crack-plane subscripts have been omitted for clarity.

The contrast between the response of a standard damage model and the new SUR damage model in 1D is illustrated in Figure 1, in which the effective stress and strain (σ_{ef} and ε_{ef} respectively) correspond to uniaxial values when the model is considered in one dimension only. Also in Figure 1, f_t denotes the uniaxial tensile strength, $\varepsilon_t = f_t/E$, E denotes Young's modulus and ε_m is the effective end of the softening curve, which experimentally equals u_m/h, where u_m = relative displacement across an FPZ at the end of the uniaxial softening curve. However; when the model was implemented in the finite element program, Bazant and Oh's [3] crack-band theory was employed, in which ε_m is computed from the fracture energy parameter (G_f) and element characteristic length (ℓ_{ch}).

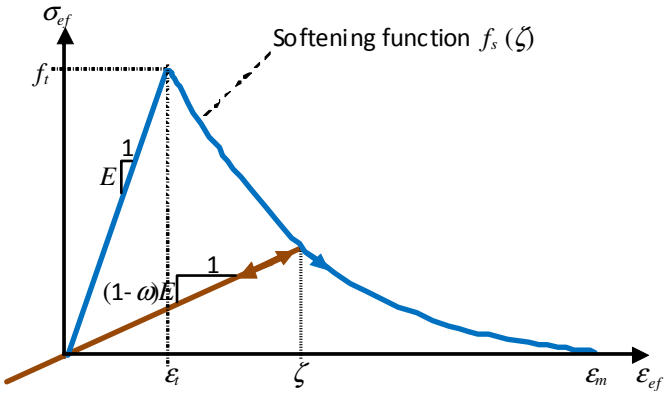

Figure 1a. Standard damage model

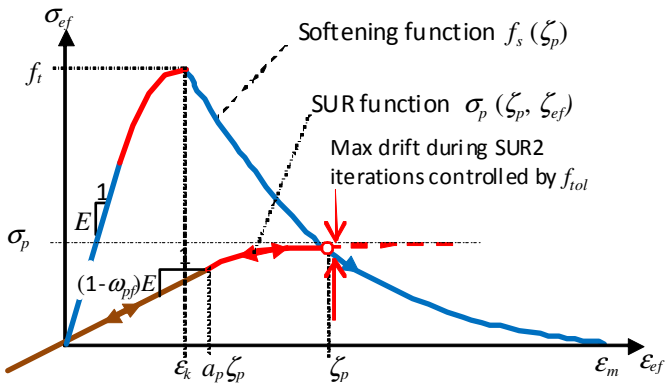

Figure 1b. SUR damage model

The counterpart to equation (3) for the SUR model is as follows;

$$\tilde{\boldsymbol{\sigma}} = \left(1 - \omega_p\left(\zeta_p, \varepsilon_{ef}\right)\right)\tilde{\mathbf{D}}\,\tilde{\boldsymbol{\varepsilon}} \tag{4}$$

in which ζ_p is the damage evolution parameter for the SUR model, which is the counterpart to ζ from the standard damage model. The crack-plane effective strain (ε_{ef}) is defined later in this paper in equation (10).

The damage parameter is now defined as follows;

$$\omega_p\left(\zeta_p,\varepsilon_{ef}\right)=\omega_{pf}=1-\frac{\sigma_k(\zeta_p)}{\upsilon E\zeta_p} \qquad \forall\ \varepsilon_{ef}\le a_p\zeta_p$$

$$\omega_p\left(\zeta_p,\varepsilon_{ef}\right)=1-\frac{\sigma_p(\zeta_p,\varepsilon_{ef})}{E\varepsilon_{ef}} \qquad \forall\ \varepsilon_{ef}> a_p\zeta_p \tag{5}$$

where the following form of the SUR function from Ref [44] is used;

$$\sigma_p\left(\zeta_p,\varepsilon_{ef}\right)=\sigma_k(\zeta_p)\left(1-\left(1-\frac{a_p}{\upsilon}\right)e^{-\frac{\varepsilon_{ef}-a_p\zeta_p}{(\upsilon-a_p)\zeta_p}}\right) \tag{6}$$

in which the constants a_p and υ take the values 0.60 and 0.75 respectively. These vary slightly from those used in Reference [44] (in which values of 0.70 and 0.75 were recommended) and were selected so that the SUR model has good compatibility with the crack contact model described below.

The asymptotic stress function ($\sigma_k(\zeta_p)$) is given by;

$$\sigma_k(\zeta_p)=f_s(\zeta_k)\,\upsilon\,a_k \qquad \forall\ \zeta_p\le\varepsilon_k$$

$$\sigma_k(\zeta_p)=f_s(\zeta_p)\,\upsilon\,a_k \qquad \forall\ \zeta_p>\varepsilon_k \tag{7}$$

noting that ε_k (=$a_k\varepsilon_t$) is the strain at the peak of the uniaxial tension curve and that the expression for a_k is defined below in equation (9).

The softening function follows a standard exponential form given by equation (8);

$$f_s(\zeta_p)=f_t \qquad \forall\ \zeta_p\le\varepsilon_k$$

$$f_s(\zeta_p)=f_t\ e^{-c_1\left(\frac{\zeta_p-\varepsilon_k}{\varepsilon_m-\varepsilon_k}\right)} \qquad \forall\ \zeta_p>\varepsilon_k \tag{8}$$

where c_1=5.

The parameter a_k is computed from the condition that $\sigma_p\left(\zeta_k,\zeta_k\right)=f_t$, which results in the following equation;

$$a_k=\frac{1}{\upsilon\cdot\left(1-\left(1-\frac{a_p}{\upsilon}\right)\cdot e^{-\left(\frac{1-a_p}{\upsilon-a_p}\right)}\right)} \tag{9}$$

We note that the strain parameter (ζ_p) is initialised to ζ_k for all crack-planes and that when $\zeta_p=\zeta_k$, f_s=f_t and ω_{pf} (from equation 5a) has the value zero.

To complete the damage formulation, a crack-plane damage function is needed. The function employed here is taken from reference [45] and is given by;

$$\varphi_d(\tilde{\boldsymbol{\varepsilon}},\zeta_p) \;=\; \varepsilon_{ef}(\tilde{\boldsymbol{\varepsilon}})-\zeta_p \;=\; \frac{\tilde{\varepsilon}_{11}}{2}\left[1+\left(\frac{\mu_\varepsilon}{r_\zeta}\right)^2\right]+\frac{1}{2{r_\zeta}^2}\sqrt{\left({r_\zeta}^2-{\mu_\varepsilon}^2\right)^2{\tilde{\varepsilon}_{11}}^2+4{r_\zeta}^2\left({\tilde{\varepsilon}_{12}}^2+{\tilde{\varepsilon}_{13}}^2\right)}-\zeta_p \qquad (10)$$

with the standard loading/unloading conditions $\dot{\zeta}_p \geq 0;\;\; \varphi_d \leq 0;\;\; \dot{\zeta}_p\varphi_d = 0;\;\; \dot{\zeta}_p\dot{\varphi}_d = 0 \;\; \forall \;\; \varphi_d = 0$

The material constants r_ζ and μ_ε are the relative shear strain intercept and the asymptotic shear friction factor respectively. These are the strain equivalents of the relative shear stress intercept $r_\sigma = c/f_t$ and the asymptotic friction factor μ, noting that c is the shear stress intercept. r_σ and μ are the input material parameters (See Summary of material properties in Table 1).

A crucial aspect of the SUR model is the method used for updating ζ_p during the incremental iterative solution procedure. For the work described in this paper, two SUR update options were used, namely SUR1 and SUR2. The first of these (SUR1) involves updating ζ_p on every iteration and at every gauss point whenever the value of ε_{ef} exceeds the value of ζ_p from the previous converged state. The second option (SUR2) involves ζ_p being frozen after a fixed number of iterations (*itx*) for each increment. However, in this latter process, the values of ε_{ef} continue to be monitored for the iterations beyond the 'fixing iteration' and a further update undertaken if ε_{ef} exceeds ζ_p and the associated value $f_s(\varepsilon_{ef})$ becomes more than tolerance value (f_{tol}) below $f_s(\zeta_p)$. For the present work, the default SUR2 parameters were set to $itx = 4$ and $f_{tol} = 0.03 f_t$. The maximum 'drift' from the softening curve possible in the second stage SUR2 iterations is illustrated in Figure 1b. Further SUR update options, as well as a detailed study on the effects of using different options, are described in Alnaas and Jefferson [44].

An important aspect of the SUR approach is that it only ever uses a positive definite stiffness matrix in the incremental-iterative solution process. For the crack-plane model alone, the 'tangent' constitutive relationship obtained from equation (4) includes only the differentials of ω_p w.r.t. ε_{ef} and not w.r.t ζ_p, thereby ensuring that the incremental matrix is positive definite as long as the function σ_p, from which ω_p is obtained, always has a positive slope, which is does.

$$\delta\tilde{\boldsymbol{\sigma}} \approx \left[\left(1-\omega_p\left(\zeta_p,\varepsilon_{ef}\right)\right)\tilde{\mathbf{D}} \;-\frac{\partial\omega_p\left(\zeta_p,\varepsilon_{ef}\right)}{\partial\varepsilon_{ef}}\tilde{\mathbf{D}}\tilde{\boldsymbol{\varepsilon}}\left(\frac{\partial\varepsilon_{ef}}{\partial\tilde{\boldsymbol{\varepsilon}}}\right)^T\right]\delta\tilde{\boldsymbol{\varepsilon}} \qquad (11)$$

Equation (11) only results in an 'exact tangent' matrix in the SUR2 approach when the number of iterations exceeds *itx* and the stress 'drift' is within the tolerance f_{tol}; however, this 'exact tangent' is with respect to the frozen nonlinear SUR function (See figure 1b) and not w.r.t. the softening function. The term 'exact tangent' is therefore not employed in the same manner as in many descriptions of standard plasticity or damage models. We emphasise that this SUR2 procedure can result in the effective stress being slightly above the softening function, but not by more than the specified tolerance (f_{tol}). The consequences of applying the SUR2 approximation are explored in the examples in section 5 of this paper.

2.3 Smoothed crack-plane contact model

The smoothed SUR approach does not simulate the closure of cracks or the effects of contact between the surfaces of rough cracks when they are loaded in shear. To enable this contact behaviour to be simulated, the stress on the damage plane is assumed to comprise an undamaged (u) and contact component (c), as follows;

$$\tilde{\boldsymbol{\sigma}} = \tilde{\boldsymbol{\sigma}}_u + \tilde{\boldsymbol{\sigma}}_c \tag{12}$$

This summation follows naturally from a local damage model. Furthermore, the implicit assumption that both stress components are governed by the same local strain vector has been found to result in a model that provides a good representation of the real damage-contact behaviour of a cracked band of material [41].

In the present case, $\tilde{\boldsymbol{\sigma}}_u$ equates to the stress from SUR damage model, given by equation (4), and $\tilde{\boldsymbol{\sigma}}_c$ will be obtained from the crack-plane contact constitutive model [41], which is now summarised.

An important component of the model is 'the effective contact function' $\varphi(\tilde{\boldsymbol{\varepsilon}})$. This function is derived from experiments in which cracks are opened under normal loading and then loaded in shear [47-49]. These experiments show that there is a definite, relatively narrow, region over which contact is regained for a given crack opening. Jefferson [50] originally interpreted the centres of these contact regions as 'contact points' and showed that the locus of these points could reasonably be represented by a conical shaped 'contact function' φ in relative-displacement, or local strain, space. Furthermore, by assigning a normal and shear stiffness to the interface, the stress developed after contact could be based on the embedment strain, defined as the nearest distance to the contact surface. In the original crack contact model [45,50], the contact was assumed to be abrupt and the cone was assumed to have a sharp apex. These assumptions were not only inconsistent with the experiments, which show that there is a gradual increase in the level of contact as surfaces move together [47-49], but also gave rise to numerical difficulties resulting from the abrupt change of stiffness when cracks closed. To remedy these deficiencies, the new model was developed that uses a smooth effective contact function and a smoothed contact transition function [41].

The effective contact function, illustrated in Figure 2, has the properties of a signed distance function in local strain space. The region names 'contact' ($\varphi(\tilde{\boldsymbol{\varepsilon}})\leq 0$) and 'no-contact' ($\varphi(\tilde{\boldsymbol{\varepsilon}})>0$) are used to describe the regions either side of $\varphi=0$.

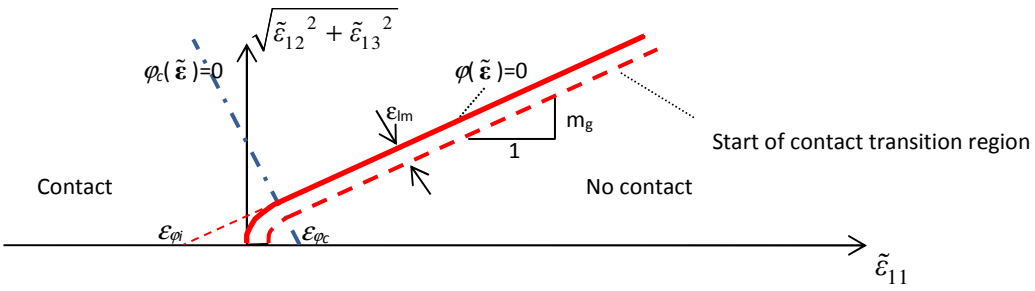

Figure 2. Effective contact surface.

The contact function ($\varphi(\tilde{\boldsymbol{\varepsilon}})$)has the following properties

$$\left|\frac{\partial \varphi}{\partial \tilde{\boldsymbol{\varepsilon}}}\right| = 1 \tag{13}$$

$$\tilde{\boldsymbol{\varepsilon}}_c = \tilde{\boldsymbol{\varepsilon}} - \phi(\tilde{\boldsymbol{\varepsilon}})\frac{\partial \varphi}{\partial \tilde{\boldsymbol{\varepsilon}}} \tag{14}$$

where $\tilde{\boldsymbol{\varepsilon}}_c$ is the local strain on the contact surface nearest to $\tilde{\boldsymbol{\varepsilon}}$, in local strain space. It is noted that equation (13) states that the magnitude of the gradient vector is unity.

$\varphi(\tilde{\boldsymbol{\varepsilon}})$ is a two-part function that comprises a section formed by a spherical arc at the apex and a section that is a partial cone which is tangential to the arc. The interface between the two functions is governed by the function φ_c, which is defined as follows:

$$\varphi_c(\tilde{\boldsymbol{\varepsilon}}) = \frac{1}{\sqrt{1+m_g{}^2}}\left(\tilde{\varepsilon}_{11} - \varepsilon_{\varphi c}(\zeta_p) + m_g\sqrt{\left(\tilde{\varepsilon}_{12}{}^2 + \tilde{\varepsilon}_{13}{}^2\right)}\right) \tag{15}$$

The effective contact function is then evaluated using:

$$\begin{aligned} \varphi &= \frac{1}{\sqrt{1+m_g{}^2}}\left(m_g \cdot \left(\tilde{\varepsilon}_{11} - \varepsilon_{\varphi i}(\zeta_p)\right) - \sqrt{\left(\tilde{\varepsilon}_{12}{}^2 + \tilde{\varepsilon}_{13}{}^2\right)}\right) \qquad \forall \quad \varphi_c(\tilde{\boldsymbol{\varepsilon}}, \zeta_p) > 0 \\ \varphi &= \varepsilon_{\varphi c}(\zeta_p) - \sqrt{\left(\left(\tilde{\varepsilon}_{11} - \varepsilon_{\varphi c}(\zeta_p)\right)^2 + \tilde{\varepsilon}_{12}{}^2 + \tilde{\varepsilon}_{13}{}^2\right)} \qquad \forall \quad \varphi_c(\tilde{\boldsymbol{\varepsilon}}, \zeta_p) \le 0 \end{aligned} \tag{16}$$

where m_g, $(\text{set to } 0.425)$ defines the slope of the conical part of the contact function, as illustrated in Figure 2.

The contact function is governed by the two parameters given in equations 17a&b. These are geometrically linked to the 'offset' strain ε_{lm} which governs the effective width of the transition region.

$$\begin{aligned} \varepsilon_{\varphi c}(\zeta_p) &= n_g\varepsilon_m + \varepsilon_{lm}(\zeta_p) \\ \varepsilon_{\varphi i}(\zeta_p) &= \frac{m_g - \sqrt{1+m_g{}^2}}{m_g}\left(n_g\varepsilon_m + \varepsilon_{lm}(\zeta_p)\right) \end{aligned} \tag{17a,b}$$

in which n_g = 0.025, the offset strain (illustrated in Figure 2) is given by;

$$\varepsilon_{lm}(\zeta_p) = \max(a_{lm}\zeta_p, a_{lm}\varepsilon_m) \tag{18}$$

in which a_{lm}=3/8

The effective contact function and associated constants were obtained by matching the contact surface to experimental data [47-49], as explained in [41].

The effective contact function is now used in the evaluation of the contact stress vector. In its most basic form, the contact stress is simply the product of damage evolution function, the elastic matrix and the local strain contact vector, i.e. $\tilde{\boldsymbol{\sigma}}_{c_basic} = \omega_p(\zeta_p)\,\tilde{\mathbf{D}}\left(\varphi\frac{d\varphi}{d\tilde{\boldsymbol{\varepsilon}}}\right)$. However, introducing the contact transition function ($\lambda_c(\varphi)$) and the offset

function (18), as well as a contact reduction function that accounts for the reduction in shear contact potential with increasing crack opening (H), gives a new form for the contact stress as follows;

$$\tilde{\boldsymbol{\sigma}}_c = \omega_p(\zeta_p)H(\tilde{\boldsymbol{\varepsilon}})\,\tilde{\mathbf{D}}\lambda_c(\varphi)\left(\left(\varphi(\tilde{\boldsymbol{\varepsilon}})-\varepsilon_{lm}\left(\zeta_p\right)\right)\frac{d\varphi}{d\tilde{\boldsymbol{\varepsilon}}}\right) \tag{19}$$

The contact transition function, given in equation (20), was derived [41] by assuming that in 1D the tangent stiffness of the crack-plane stress-strain relationship for a closing crack follows a tanh function in terms of φ. Integrating the tanh function gave a constant which was related to the offset strain (ε_{lm}). This was then calibrated against data from Reinhardt's tests [51].

$$\lambda_c(\varphi)=\frac{1}{2}\left[1-\frac{\varphi}{\varphi-\varepsilon_{lm}}\ln\left(\frac{cosh\left(\varphi/\varepsilon_z\right)}{cosh\left(\varepsilon_{lm}\right)}\right)\right] \tag{20}$$

in which $\varepsilon_z=\varepsilon_{lm}/c_{lm}$

The basic contact reduction function [41] is defined as follows;

$$\begin{aligned} H_0(\tilde{\varepsilon}_1)&=\sum_{i=1}^{3} p_i e^{-(\tilde{\varepsilon}_1-\varepsilon_k)/(c_i\varepsilon_m)} && \forall \quad \tilde{\varepsilon}_1 \geq \varepsilon_k \\ H_0(\tilde{\varepsilon}_1)&=1 && \forall \quad \tilde{\varepsilon}_1 < \varepsilon_k \end{aligned} \tag{21}$$

where typically p = [0.6, 0.3, 0.1]^T and c=[0.01, 0.05, 2.0]^T, noting that the parameters are written as vectors for convenience. The material parameters p_1,p_2,p_3 nominally represent the proportions of shear transfer associated with the hardened cement paste (hcp), fine and coarse aggregate phases respectively and satisfy the condition $\sum p_i$=1 . c_i (i=1 to 3) are associated parameters that are determined from shear-normal tests on cracked concrete specimens, as explained in reference [41]. In this work, c_i are fixed at the values given and the only rough contact material parameters that are permitted to vary are p_i but, because they sum to unity, only two of the parameters (p_i) need be set. We chose p_2 and p_3 to be model parameters.

When the model is applied to continuum elements using the smeared crack approach it is necessary to scale the contact reduction function in order to ensure that the shear response of cracked elements is mesh invariant. The resulting element-size dependent function was proved in reference [41] to be;

$$H(\eta_H)=\frac{H_0(\eta_H)\ell_{ch}}{H_0(\eta_H)\ell_{ch}+\left(1-H_0(\eta_H)\right)h} \tag{22}$$

where $\eta_H(\tilde{\boldsymbol{\varepsilon}})=\left(\frac{\tilde{\varepsilon}_{11}-\varepsilon_k}{\varepsilon_m}\right)$

As mentioned in [41], the need to scale crack shear relationships has been overlooked in much work that has employed smeared crack models.

2.4 Combined crack-plane constitutive relationship

The final crack-plane relationship is obtained by equating $\tilde{\boldsymbol{\sigma}}$ from (4) to $\tilde{\boldsymbol{\sigma}}_u$ in (12) and by using $\tilde{\boldsymbol{\sigma}}_c$ from (19) in (12) as follows;

$$\tilde{\boldsymbol{\sigma}} = \left(1-\omega_p\left(\zeta_p, \varepsilon_{ef}\right)\right)\tilde{\mathbf{D}}\,\tilde{\boldsymbol{\varepsilon}} + \omega_p(\zeta_p)H(\tilde{\boldsymbol{\varepsilon}})\,\tilde{\mathbf{D}}\lambda_c(\varphi)\cdot\left(\left(\varphi(\tilde{\boldsymbol{\varepsilon}}) - \varepsilon_{lm}\left(\zeta_p\right)\right)\frac{d\varphi}{d\tilde{\boldsymbol{\varepsilon}}}\right) \tag{23}$$

For convenience equation (23) is rewritten as;

$$\tilde{\boldsymbol{\sigma}} = \tilde{\mathbf{D}}\,\mathbf{M}_s\tilde{\boldsymbol{\varepsilon}} + \tilde{\mathbf{D}}\tilde{\boldsymbol{\varepsilon}}_s \tag{24}$$

where $\mathbf{M}_s = \left(1-\omega_p\right)\mathbf{I}$ and $\tilde{\boldsymbol{\varepsilon}}_s = \omega_p H\ \lambda_c\cdot\left(\left(\varphi-\varepsilon_{lm}\right)\frac{d\varphi}{d\tilde{\boldsymbol{\varepsilon}}}\right)$

3. COUPLING THE CRACK-PLANE MODEL WITH CONTINUUM PLASTICITY

3.1 Continuum plasticity model component

The plasticity model component of the present combined plastic-damage-contact model uses the 3D yield function ($F(\boldsymbol{\sigma}, Z(\kappa))$), plastic potential ($G(\boldsymbol{\sigma}, Z(\kappa))$) and hardening function $Z(\kappa)$ from References [44] and [45]. The latter function depends on the pressure-dependent work hardening parameter (κ). All of these functions, and associated material parameters, are given in Appendix A.

3.2 Combining the plasticity and crack-plane model components

The Cartesian stress-strain relationship is given by;

$$\boldsymbol{\sigma} = \mathbf{D}_e\left(\boldsymbol{\varepsilon} - \boldsymbol{\varepsilon}_p - \boldsymbol{\varepsilon}_f\right) \tag{25}$$

where $\boldsymbol{\varepsilon}_f$ denotes the summed fracture strain and $\boldsymbol{\varepsilon}_p$ is the plastic strain.

The following three assumptions are employed to link the crack-plane stress-strain relationship to the Cartesian (or overall) constitutive equation.

1. The fracture strain is the sum of the transformed inelastic strain components from all cracks at a particular point, which is given by;

$$\boldsymbol{\varepsilon}_f = \sum_{j=1}^{n_p} \mathbf{N}_j{}^{\mathrm{T}}\breve{\boldsymbol{\varepsilon}}_j \tag{26}$$

   in which $\mathbf{N}$ is the stress transformation matrix ($\mathbf{N}^{\mathrm{T}}$ giving transformed strains) and *j* is the crack-plane number.

2. The crack-plane stress is equal to the transformed Cartesian stress. This is also known as the 'static constraint', which for crack-plane *j* is given by;

$$\tilde{\boldsymbol{\sigma}}_j = \mathbf{N}(\mathbf{r}^j)\boldsymbol{\sigma} \tag{27}$$

3. The inelastic crack-plane strain ($\breve{\boldsymbol{\varepsilon}}$) may be obtained by subtracting the elastic component of the crack-plane strain from the total crack-plane strain as follows, noting that crack-plane suffixes have now been dropped for clarity;

$$\breve{\boldsymbol{\varepsilon}} = \tilde{\boldsymbol{\varepsilon}} - \tilde{\mathbf{D}}^{-1}\tilde{\boldsymbol{\sigma}} \tag{28}$$

Substituting for $\tilde{\boldsymbol{\varepsilon}}$ in (28) from (24) gives;

$$\breve{\boldsymbol{\varepsilon}} = \mathbf{M}_s{}^{-1}\tilde{\mathbf{D}}^{-1}\left(\tilde{\boldsymbol{\sigma}} - \tilde{\mathbf{D}}\tilde{\boldsymbol{\varepsilon}}_s\right) - \tilde{\mathbf{D}}^{-1}\tilde{\boldsymbol{\sigma}} \tag{29}$$

(29) may be further rearranged to give;

$$\breve{\boldsymbol{\varepsilon}} = \tilde{\mathbf{C}}_s\tilde{\boldsymbol{\sigma}} - \mathbf{M}_s{}^{-1}\tilde{\boldsymbol{\varepsilon}}_s \tag{30}$$

in which $\mathbf{C}_s = \left(\mathbf{M}_s{}^{-1} - \mathbf{I}\right)\tilde{\mathbf{C}}$ and $\mathbf{C} = \tilde{\mathbf{D}}^{-1}$

alternatively, substituting for $\tilde{\boldsymbol{\sigma}}$ in (28) using (24) and rearranging results in;

$$\breve{\boldsymbol{\varepsilon}} = \left(\mathbf{I} - \mathbf{M}_s\right)\tilde{\boldsymbol{\varepsilon}} + \tilde{\boldsymbol{\varepsilon}}_s \tag{31}$$

Using (24), (26) and (30) in equation (25) gives the final form of the Cartesian stress-strain relationship;

$$\boldsymbol{\sigma} = \left(\mathbf{I} + \mathbf{D}_e \sum_{j=1}^{n_p} \mathbf{N}_j{}^{\mathrm{T}}\tilde{\mathbf{C}}_{s_j}\mathbf{N}_j\right)^{-1} \mathbf{D}_e\left(\left(\boldsymbol{\varepsilon} - \boldsymbol{\varepsilon}_p\right) + \sum_{j=1}^{n_p} \mathbf{N}_j{}^{\mathrm{T}}\mathbf{M}_{s_j}^{-1}\tilde{\boldsymbol{\varepsilon}}_{s_j}\right) \tag{32}$$

Although equation (32), along with its dependent functions, fully defines the constitutive relationship, a solution algorithm is required to make the model useable. An approach that includes a consistent tangent matrix and closest point projection (CPP) algorithm [52] has been developed for implementing the model in a finite element code. The principles used to develop the algorithm follow those described in [46] but the introduction of the SUR and smooth contact approaches into the model has necessitated some very significant changes. The algorithm used to compute the stress and the details of the 'tangent' stiffness matrix will now be described in the following sub-sections.

3.3. Calculation of stresses using a CPP approach

The solution algorithm is developed in the context of an incremental-iterative Newton type solution. Differential relationships will be applied during iterations and differential quantities denoted by δ. The total change of a variable during an increment, from the last converged state, is denoted by Δ.

At every iteration, the strain at the last converged state ($\boldsymbol{\varepsilon}_{lcs}$) will be known and the increment of strain from this converged strain will also be available ($\Delta\boldsymbol{\varepsilon}$). The aim of the stress algorithm is then to compute the new stress associated with the strain ($\boldsymbol{\varepsilon}_{lcs}+\Delta\boldsymbol{\varepsilon}$). This involves first checking for any new cracks, forming them as necessary, and then updating the crack-plane and plastic variables for all cracks and yield conditions as required. A principal stress criterion is used for crack formation and the formation of cracks is systematically checked one at a time during the overall stress recovery procedure.

Once the number of cracks is known, a CPP algorithm is used to compute the stress. This is outlined in the remainder of this subsection in which it is assumed that there is at least one crack and that plasticity is active. The aim of the CPP algorithm is to compute stresses which satisfy the yield function, the static constraint, plastic strain error condition and work hardening parameter error condition, as given in equations (33) to (36) respectively.

$$F\left(\boldsymbol{\sigma},\kappa\right)=0 \tag{33}$$

$$\boldsymbol{\psi}_j=\mathbf{N}_j\boldsymbol{\sigma}-\tilde{\mathbf{D}}_j\left(\mathbf{M}_{s_j}\tilde{\boldsymbol{\varepsilon}}_j+\tilde{\boldsymbol{\varepsilon}}_{s_j}\right)=\mathbf{0} \tag{34}$$

$$\mathbf{R}_{\varepsilon}=-\Delta\boldsymbol{\varepsilon}_p+\frac{\partial G}{\partial\boldsymbol{\sigma}}\Delta\lambda=\mathbf{0} \tag{35}$$

$$R_{\kappa}=-\Delta\kappa+X\,\Delta\lambda\;\boldsymbol{\sigma}^T\frac{\partial G}{\partial\boldsymbol{\sigma}}=0 \tag{36}$$

in which λ is the plastic multiplier and X is the ductility parameter defined in Appendix A.

A trial stress will generally result in some or all of the above functions being nonzero and a Newton-Raphson solution is employed to solve a set of coupled equations such that all four conditions are satisfied to within defined tolerances (see Box 1). To derive these coupled equations, we start by expanding (36), such that $R_{\kappa}+\delta R_{\kappa}=0$, and rearranging the result to obtain the following expression for $\delta\kappa$:

$$\delta\kappa=a_{\kappa}\left(R_{\kappa}+\Delta\lambda\mathbf{k}_{\sigma}{}^T\delta\boldsymbol{\sigma}+c_{\kappa}\delta\lambda\right) \tag{37}$$

in which $a_{\kappa}=\left(1-\Delta\lambda X\boldsymbol{\sigma}^T\frac{\partial^2 G}{\partial\boldsymbol{\sigma}\partial d\kappa}\right)^{-1}$, $\quad c_{\kappa}=X\boldsymbol{\sigma}^T\frac{\partial G}{\partial\boldsymbol{\sigma}}$ and $\mathbf{k}_{\sigma}=X\cdot\left(\frac{\partial G}{\partial\boldsymbol{\sigma}}+\frac{\partial^2 G}{\partial\boldsymbol{\sigma}^2}\boldsymbol{\sigma}\right)$.

Undertaking a similar process for equation (35) gives the following equation for $\delta\boldsymbol{\varepsilon}_p$;

$$\delta\boldsymbol{\varepsilon}_p=\left(\mathbf{R}_{\varepsilon}+\Delta\lambda\frac{\partial^2 G}{\partial\boldsymbol{\sigma}\partial\kappa}a_{\kappa}R_{\kappa}\right)+\delta\lambda\left(\frac{\partial G}{\partial\boldsymbol{\sigma}}+\Delta\lambda\frac{\partial^2 G}{\partial\boldsymbol{\sigma}\partial\kappa}a_{\kappa}c_{\kappa}\right)+\left(\Delta\lambda\frac{\partial^2 G}{\partial\boldsymbol{\sigma}^2}+\Delta\lambda\frac{\partial^2 G}{\partial\boldsymbol{\sigma}\partial\kappa}a_{\kappa}\Delta\lambda\mathbf{k}_{\sigma}{}^T\right)\delta\boldsymbol{\sigma} \tag{38}$$

The yield function consistency condition, derived from (33), may be written;

$$F+\frac{\partial F}{\partial\boldsymbol{\sigma}}^T\delta\boldsymbol{\sigma}+\frac{\partial F}{\partial\kappa}\delta\kappa=0 \tag{39}$$

Noting that F is the value of the yield function with the most recent non-converged value of $\boldsymbol{\sigma}$.

Substituting for $\delta\kappa$ from (37) and grouping terms that pre-multiply $\delta\boldsymbol{\sigma}$ results in;

$$F+\mathbf{f}_{\kappa}{}^T\delta\boldsymbol{\sigma}+\frac{\partial F}{\partial\kappa}a_{\kappa}R_{\kappa}+h_{\kappa}\delta\lambda=0 \tag{40}$$

where $\mathbf{f}_{\kappa}=\frac{\partial F}{\partial\boldsymbol{\sigma}}+\frac{\partial F}{\partial\kappa}a_{\kappa}\Delta\lambda\mathbf{k}_{\sigma}$ and $h_{\kappa}=\frac{\partial F}{\partial\kappa}a_{\kappa}c_{\kappa}$

Expanding the static constraint as $\boldsymbol{\psi}_j+\delta\boldsymbol{\psi}_j=\mathbf{0}$ gives;

$$\boldsymbol{\psi}_j+\mathbf{N}_j\delta\boldsymbol{\sigma}-\tilde{\mathbf{D}}_{t_j}\delta\tilde{\boldsymbol{\varepsilon}}_j=\mathbf{0} \tag{41}$$

in which $\tilde{\mathbf{D}}_{t_j} = \tilde{\mathbf{D}}\mathbf{M}'_{s_j}$, $\mathbf{M}'_{s_j} = \left(\mathbf{M}_{s_j} + \frac{\partial \mathbf{M}_{s_j}}{\partial \tilde{\boldsymbol{\varepsilon}}_j} \circ \tilde{\boldsymbol{\varepsilon}}_j + \frac{\partial \tilde{\boldsymbol{\varepsilon}}_{s_j}}{\partial \tilde{\boldsymbol{\varepsilon}}_j} \right)$ and $\circ$ denotes a third-order-matrix vector contraction.

The first trial stress is given by;

$$\boldsymbol{\sigma} = \mathbf{D}_e \left(\boldsymbol{\varepsilon} + \Delta\boldsymbol{\varepsilon} - \boldsymbol{\varepsilon}_p - \sum_{j=1}^{n_p} \mathbf{N}_j{}^{\mathrm{T}} \breve{\boldsymbol{\varepsilon}}_j \right) \tag{42}$$

in which $\boldsymbol{\varepsilon}$, $\boldsymbol{\varepsilon}_p$ and $\breve{\boldsymbol{\varepsilon}}$ are all values from the last converged state, $\breve{\boldsymbol{\varepsilon}}$ being computed from the stored values of $\tilde{\boldsymbol{\varepsilon}}$ and equation (31).

Iterations are performed to satisfy equations (33) to (36) and during these stress-update iterations the total strain tensor does not change, therefore the iterative change in the stress is given by;

$$\delta\boldsymbol{\sigma} = -\mathbf{D}_e \left(\delta\boldsymbol{\varepsilon}_p + \sum_{j=1}^{n_p} \mathbf{N}_j{}^{\mathrm{T}} \delta\breve{\boldsymbol{\varepsilon}}_j \right) \tag{43}$$

The unknowns in (34) are the crack-plane strains whereas it is the crack-plane fracture strains that appear in (43). We chose to solve for $\tilde{\boldsymbol{\varepsilon}}$ since these do not vanish when cracks are fully closed.

The relationship between the differential strains $\delta\tilde{\boldsymbol{\varepsilon}}$ and $\delta\breve{\boldsymbol{\varepsilon}}$ may be derived from (24) and (31) to be;

$$\delta\breve{\boldsymbol{\varepsilon}}_j = \left(\mathbf{I} - \mathbf{M}'_{s_j} \right) \delta\tilde{\boldsymbol{\varepsilon}}_j \tag{44}$$

The next stage in the derivation involves replacing $\delta\boldsymbol{\varepsilon}_p$ and $\delta\breve{\boldsymbol{\varepsilon}}$, from (38) and (44) respectively, in (43)and rearranging to obtain;

$$\delta\boldsymbol{\sigma} = -\mathbf{A}_e \left(\mathbf{R}_{\varepsilon\kappa} + \delta\lambda \mathbf{g}_m + \sum_{j=1}^{n_p} \mathbf{N}_j{}^{\mathrm{T}} \left(\mathbf{I} - \mathbf{M}'_{s_j} \right) \delta\tilde{\boldsymbol{\varepsilon}}_j \right) \tag{45}$$

in which $\mathbf{A}_e = \left(\mathbf{I} + \Delta\lambda \mathbf{D}_e \left(\frac{\partial^2 G}{\partial \boldsymbol{\sigma}^2} + \frac{\partial^2 G}{\partial \boldsymbol{\sigma} \partial \kappa} a_\kappa \Delta\lambda \mathbf{k}_\sigma{}^{\mathrm{T}} \right) \right)^{-1} \mathbf{D}_e$

Substituting for $\delta\boldsymbol{\sigma}$ from (45) into (40) and (41), and rearranging gives the following set of coupled equations;

$$\begin{aligned} F_\lambda &= M_\lambda \delta\lambda + \mathbf{b}_{\lambda_k} \delta\tilde{\boldsymbol{\varepsilon}}_k \\ \boldsymbol{\psi}_{Ej} &= \mathbf{m}_{E_j} \delta\lambda + \mathbf{B}_{E_{j,k}} \delta\tilde{\boldsymbol{\varepsilon}}_k \end{aligned} \tag{46}$$

in which both j and k are crack plane indices from 1 to n_p.

$$F_\lambda = F + \frac{\partial F}{\partial \kappa} a_\kappa R_\kappa - \mathbf{f}_\kappa{}^{\mathrm{T}} \mathbf{A}_e \mathbf{R}_{\varepsilon\kappa} \qquad \boldsymbol{\psi}_{E_j} = \boldsymbol{\psi}_j - \mathbf{N}_j \mathbf{A}_e \mathbf{R}_{\varepsilon\kappa}$$

$$M_\lambda = \mathbf{f}_\kappa{}^{\mathrm{T}} \mathbf{A}_e \mathbf{g}_m - h_\kappa \qquad \mathbf{m}_{E_j} = \mathbf{N}_j \mathbf{A}_e \mathbf{g}_m$$

$$\mathbf{b}_{\lambda_k} = \mathbf{f}_\kappa{}^{\mathrm{T}} \mathbf{A}_e \mathbf{N}_k{}^{\mathrm{T}} \left(\mathbf{I} - \mathbf{M}'_{s_k} \right) \qquad \mathbf{B}_{E_{j,k}} = \mathbf{N}_j \mathbf{A}_e \mathbf{N}_k{}^{\mathrm{T}} \left(\mathbf{I} - \mathbf{M}'_{s_k} \right) + \tilde{\mathbf{D}}_{t_{j,k}} \partial_{j,k}$$

where $\partial_{i,j}$ is Kronecker's delta, $\mathbf{R}_{\varepsilon\kappa} = \left(\mathbf{R}_\varepsilon + \Delta\lambda \frac{\partial^2 G}{\partial \boldsymbol{\sigma} \partial \kappa} a_\kappa R_\kappa \right)$ and $\mathbf{g}_m = \frac{\partial G}{\partial \boldsymbol{\sigma}} + \Delta\lambda \frac{\partial^2 G}{\partial \boldsymbol{\sigma} \partial \kappa} a_\kappa c_\kappa$

For a particular case in which plasticity and two cracks are active, (46) takes the following form;

$$\begin{bmatrix} F_\lambda \\ \boldsymbol{\psi}_{E_1} \\ \boldsymbol{\psi}_{E_2} \end{bmatrix} = \begin{bmatrix} M_\lambda & \mathbf{b}_{\lambda 1} & \mathbf{b}_{\lambda 2} \\ \mathbf{m}_{E_1} & \mathbf{B}_{E_{1,1}} & \mathbf{B}_{E_{1,2}} \\ \mathbf{m}_{E_2} & \mathbf{B}_{E_{2,1}} & \mathbf{B}_{E_{2,2}} \end{bmatrix} \begin{bmatrix} \delta\lambda \\ \delta\tilde{\boldsymbol{\varepsilon}}_1 \\ \delta\tilde{\boldsymbol{\varepsilon}}_2 \end{bmatrix} \tag{47}$$

which is alternatively written as the following single matrix equation and in which the vectors and matrix correspond directly to those in (47);

$$\boldsymbol{\Gamma} = \boldsymbol{\Xi}\ \delta\boldsymbol{\Lambda} \tag{48}$$

The return mapping algorithm is now summarised in Box 1.

Box 1. Return-mapping algorithm

Step	Description
1	Initialize $\Delta\lambda = 0$ and $\Delta\kappa = 0$,
2	Compute trial stress from $\boldsymbol{\sigma} = \mathbf{D}_e\left(\boldsymbol{\varepsilon} - \boldsymbol{\varepsilon}_p - \sum_{j=1}^{n_p} \mathbf{N}_j{}^{\mathrm{T}}\left(\left(\mathbf{I} - \mathbf{M}_{s_j}\right)\tilde{\boldsymbol{\varepsilon}}_j + \tilde{\boldsymbol{\varepsilon}}_{s_j}\right)\right)$ (i.e. equation 42 and 31)
3	Evaluate $\boldsymbol{\Gamma}$ and $\boldsymbol{\Xi}$ from (48) and solve for $\delta\boldsymbol{\Lambda}$ (which gives $\delta\lambda$ and $\delta\tilde{\boldsymbol{\varepsilon}}_j$)
4	Update $\tilde{\boldsymbol{\varepsilon}}_j$ and ζ_{p_j}
5	Compute $\delta\boldsymbol{\sigma}$ from (43)
6	Compute $\delta\kappa$ and $\delta\boldsymbol{\varepsilon}_p$ from (37) and (38) respectively
7	Update plastic terms $\boldsymbol{\varepsilon}_p = \boldsymbol{\varepsilon}_p + \delta\boldsymbol{\varepsilon}_p;\ \Delta\boldsymbol{\varepsilon}_p = \Delta\boldsymbol{\varepsilon}_p + \delta\boldsymbol{\varepsilon}_p;\ \Delta\lambda = \Delta\lambda + \delta\lambda;\ \Delta\kappa = \Delta\kappa + \delta\kappa;\ \kappa = \kappa + \delta\kappa$
8	Compute a new trial stress from $\boldsymbol{\sigma} = \mathbf{D}_e\left(\boldsymbol{\varepsilon} - \boldsymbol{\varepsilon}_p - \sum_{j=1}^{n_p} \mathbf{N}_j{}^{\mathrm{T}}\left(\left(\mathbf{I} - \mathbf{M}_{s_j}\right)\tilde{\boldsymbol{\varepsilon}}_j + \tilde{\boldsymbol{\varepsilon}}_{s_j}\right)\right)$
9	Compute F and $\boldsymbol{\psi}_j$, $\mathbf{R}_\varepsilon$, R_κ from (33-36)
10	Check for convergence i.e. if $\lvert F\rvert \le \sigma_{tol};\quad \lvert\boldsymbol{\psi}\rvert \le \sigma_{tol};\quad \lvert\mathbf{R}_\varepsilon\rvert \le \varepsilon_{tol};\ R_\kappa \le \varepsilon_{tol}$ If all satisfied then exit CPP loop, else return to Step 3 [1]

1. Tolerance levels are $\varepsilon_{tol} = \varepsilon_t * 10^{-6}$ $\sigma_{tol} = f_t * 10^{-6}$

Attention now turns to the tangent matrix that is consistent with this CPP algorithm.

3.4 Consistent tangent matrix

To derive the consistent tangent matrix we start by taking the incremental form of equation (25) and making use of (26), as follows;

$$\delta\boldsymbol{\sigma} = \mathbf{D}_e\left(\delta\boldsymbol{\varepsilon} - \delta\boldsymbol{\varepsilon}_p - \sum_{j=1}^{n_p}\left(\mathbf{N}_j{}^{\mathrm{T}}\delta\tilde{\boldsymbol{\varepsilon}}_j + \delta\mathbf{N}_j{}^{\mathrm{T}}\tilde{\boldsymbol{\varepsilon}}_j\right)\right) \tag{49}$$

In the present approach, $\delta\mathbf{N}_j$ is set to **0**. This is considered reasonable because crack directions are fixed after a prescribed number of iterations (*itf*=*3*) in each increment.

The incremental local fracture strains are derived from the differential form of (24), which may be derived to be;

$$\delta\tilde{\boldsymbol{\sigma}} = \tilde{\mathbf{D}}\mathbf{M}_s{}'\delta\tilde{\boldsymbol{\varepsilon}} \tag{50}$$

The incremental fracture strains are then given by equation (51);

$$\delta\tilde{\boldsymbol{\varepsilon}} = \delta\tilde{\boldsymbol{\varepsilon}} - \tilde{\mathbf{D}}^{-1}\delta\tilde{\boldsymbol{\sigma}} = \left(\mathbf{M}_s{}'^{-1} - \mathbf{I}\right)\tilde{\mathbf{C}}\delta\tilde{\boldsymbol{\sigma}} = \tilde{\mathbf{C}}'\delta\tilde{\boldsymbol{\sigma}} \tag{51}$$

Focusing now the plasticity component of the model, for which the increments of the hardening parameter and plastic strain are given by equations (52) and (53) respectively;

$$\delta\kappa = a_\kappa \left(\Delta\lambda \mathbf{k}_\sigma{}^T d\boldsymbol{\sigma} + c_\kappa \delta\lambda \right) \tag{52}$$

$$\delta\boldsymbol{\varepsilon}_p = \delta\lambda \frac{\partial G}{\partial \boldsymbol{\sigma}} + \Delta\lambda \frac{\partial^2 G}{\partial \boldsymbol{\sigma}^2} \delta\boldsymbol{\sigma} + \Delta\lambda \frac{\partial^2 G}{\partial \boldsymbol{\sigma} \partial \kappa} \delta\kappa \tag{53}$$

Using (52) in (53) gives the following form for the incremental plastic strain;

$$\delta\boldsymbol{\varepsilon}_p = \delta\lambda \mathbf{g}_m + \Delta\lambda \mathbf{G}_{\boldsymbol{\sigma\kappa}} \delta\boldsymbol{\sigma} \tag{54}$$

where $\mathbf{G}_{2\sigma\kappa} = \left(\frac{\partial^2 G}{\partial \boldsymbol{\sigma}^2} + \frac{\partial^2 G}{\partial \boldsymbol{\sigma} \partial \kappa} a_\kappa \Delta\lambda \mathbf{k}_\sigma{}^T \right)$ and $\mathbf{g}_m = \frac{\partial G}{\partial \boldsymbol{\sigma}} + \Delta\lambda \frac{\partial^2 G}{\partial \boldsymbol{\sigma} \partial \kappa} a_\kappa c_\kappa$

Substituting for the differential plastic strain from (54) and the differential crack-plane fracture strain from (51) into (49), using (27) in incremental form and remembering that $\delta\mathbf{N}$ is **0**, results in the following;

$$\delta\boldsymbol{\sigma} = \mathbf{D}_e \left(\delta\boldsymbol{\varepsilon} - \left(\delta\lambda \mathbf{g}_m + \Delta\lambda \mathbf{G}_{\boldsymbol{\sigma\kappa}} \delta\boldsymbol{\sigma} \right) - \sum_{j=1}^{n_p} \mathbf{N}_j{}^{\mathrm{T}} \tilde{\mathbf{C}}'_j \mathbf{N}_j \delta\boldsymbol{\sigma} \right) \tag{55}$$

(55) may be rearranged into the form shown in (56).

$$\delta\boldsymbol{\sigma} = \mathbf{A}_c \left(\delta\boldsymbol{\varepsilon} - \delta\lambda \mathbf{g}_m \right) \tag{56}$$

in which

$$\mathbf{A}_c = \left(\mathbf{I} + \mathbf{D}_e \left(\Delta\lambda \mathbf{G}_{2\sigma\kappa} + \sum_{j=1}^{n_p} \mathbf{N}_j{}^T \tilde{\mathbf{C}}'_j \mathbf{N}_j \right) \right)^{-1} \mathbf{D}_e$$

Using the consistency condition for the yield surface gives;

$$\delta F = \mathbf{f}_\kappa{}^T \delta\boldsymbol{\sigma} + h_\kappa \delta\lambda = 0 \tag{57}$$

from which an expression for $\delta\lambda$ is derived as follows;

$$\delta\lambda = \frac{\mathbf{f}_\kappa{}^T \mathbf{A}_c \delta\boldsymbol{\varepsilon}}{\left(\mathbf{f}_\kappa{}^T \mathbf{A}_c \mathbf{g}_m - h_\kappa \right)} \tag{58}$$

in which $h_\kappa = \frac{\partial F}{\partial \kappa} a_\kappa c_\kappa$

Finally, substituting for $\delta\lambda$ from (58) into (56) and rearranging gives the following tangential stress–strain relationship;

$$\delta\boldsymbol{\sigma} = \left[\mathbf{A}_c - \frac{\mathbf{A}_c \mathbf{g}_m \mathbf{f}_\kappa{}^T \mathbf{A}_c}{\mathbf{f}_\kappa{}^T \mathbf{A}_c \mathbf{g}_m - h_\kappa} \right] \delta\boldsymbol{\varepsilon} \tag{59}$$

The matrix (in square brackets) shown in equation (59) is used in the finite element program to form the tangent stiffness matrix in the standard way [32,33].

4. MATERIAL AND SOLUTION PARAMETERS

The constitutive model described in the preceding sections contains quite a few material parameters. These include standard elastic constants, parameters obtained from uniaxial, biaxial and triaxial compression tests, as well as fracture tests. Table 1 gives a summary of the material parameters, typical values and guidance on how they can be obtained.

Table 1. Material parameters

Symbol	Description	Typical values for concrete	Comments / Relevant section of paper
E	Young's modulus.	35000 N/mm^2	Standard elastic material constant
ν	Poisson's ratio	0.2	Standard elastic material constant
f_c	Uniaxial compressive strength	40 N/mm^2	Standard material strength parameter
f_t	Uniaxial tensile strength	3 N/mm^2	Standard material strength parameter
ε_c	Strain at peak uniaxial compression	0.0022	Standard material parameter obtained form uniaxial compression tests. Appendix A.
G_f	Fracture energy per unit area.	0.1 N/mm	Standard material parameter obtained from notched fracture tests [3,54]. Section 2.2
b_r	Biaxial to uniaxial peak principal stress ratio	1.15	Common parameter obtained from biaxial compression tests [54]. Section 3.1 & Appendix A.
Z_0	Initial value of friction hardening variable	0.6	Obtained from triaxial compression tests [54-55]. Section 3.1 & Appendix A.
ψ	Dilatancy factor giving plastic potential slope relative to that of yield surface	-0.1	Obtained from triaxial compression tests [55]. Section 3.1 & Appendix A.
m_g	Constant in interlock state function	0.425	Governs slope of the contact surface cone. Obtained from tests in which shear loading is applied to specimens with fully formed cracks at different opening displacements. [47-49]. Section 2.3.
$[p_2,p_3]$	Shear contact proportion parameters	[0.3, 0.1]	p_i $(i=1$ to $3)$nominally represent the proportions of shear transfer associated with the hcp, fine and coarse aggregate phases respectively. p_i can calibrated using tests in which cracks are opened under normal loading and then loaded in shear. [47-49]. Section 2.3. Note: $p_1 = 1-p_2-p_3$.
r_σ	Shear intercept to tensile strength ratio for local damage surface	1.25	Obtained from shear tests on aggregate-hcp interfaces by inversely identifying parameters that accurately represent crack growth under mixed mode conditions. Standard values taken from [45]. Section 2.3
μ	Limiting friction ratio on which damage surface is based	0.8	
h	Physical fracture process zone width (i.e. 3x coarse aggregate size)	60mm	Based on the size of the coarse aggregate. Section 2.2.

5. EXAMPLES

The material model described in this paper has been implemented in finite element program LUSAS [62] and used to produce all of the examples presented this section.

The examples include an illustrative single element example, the analysis of plain concrete samples and the simulation of some reinforced concrete structural elements. These examples examine the mesh convergence properties of the model, as well as exploring the ability of the model to predict pre- and post-peak responses and failure modes of both plain and reinforced concrete structural elements.

The material parameters used for each of the examples are given in Tables 2 and 3. Table 3 also includes the convergence tolerance adopted. A Newton-based incremental iterative scheme was used to solve the nonlinear finite element equations and the convergence tolerances (Ψ_d, Ψ_f) relate to the L2 iterative displacement and out of balance force norms respectively. All 2D meshes comprised bilinear quadrilateral elements and the 3D mesh used trilinear hexahedral elements. The size of the load/displacement increments used in each example is evident from the response curve graphs, in which markers show the result at each increment solved. The solutions presented were obtain with option SUR2 unless noted otherwise.

Table 2. Concrete material properties

Ex	E GPa	ν	f_c MPa	f_t MPa	ε_c	G_f N/mm	b_c	Z_0	ψ	m_g	p_2 p_3	r_σ	μ	h mm
1	35	0.2	40.0	3.0	0.0022	0.10	1.15	0.6	-0.1	0.425	0.3 0.1	1.25	0.8	60
2	35	0.2	40.0	3.0	0.0022	0.10	1.15	0.6	-0.1	0.425	0.3 0.1	1.25	0.8	30
3	38	0.2	40.0	2.5	0.0018	0.075	1.15	0.6	-0.1	0.425	0.3 0.1	1.25	0.8	30
4	22.5	0.2	25.0	2.5	0.0018	0.12	1.15	0.6	-0.1	0.425	0.3 0.2	1.25	0.8	60
5	37	0.12	52.6	3.1	0.0024	0.12	1.15	0.6	-0.1	0.425	0.3 0.2	1.25	1.0	60

Table 3. Reinforcement properties and convergence tolerances

Ex.	E_s GPa	f_y MPa	H_y GPa	ε_m		Ψ_d %	Ψ_f %
1	-	-	-	-		0.1	0.1
2	-	-	-	-		0.0001*	0.0001*
3	-	-	-	-		0.1	0.1
4	205	556	2	0.03		0.1	0.1
5	210	484	4	0.03		0.1	0.1

f_y=yield stress, H_y =hardening modulus, ε_m= the strain limit for hardening
*Tighter tolerance used for SUR option comparison only

Example 1. Single element tests

Example 1 considers a 100mm cube of concrete and simulates the response under 3 different displacement paths using a single 8-noded hexahedral element. The purpose of this example is to illustrate the constitutive behaviour of the model for paths that involve cracking, crack closing, crack contact in shear, crushing in compression and crack formation in shear under constrained conditions.

The paths considered are explained in Figure 3 and the results presented in Figures 4 to 6. The responses are not compared to any experimental data but are purely for illustrative purposes. In all cases the smooth response of the model predictions is evident. We note that the sign of the minor principal stress has been reversed in the graph in Figure 6 and that the peak value exceeds f_c because the element is confined (i.e. $\varepsilon_{xx}=\varepsilon_{yy}=\varepsilon_{zz}=0$).

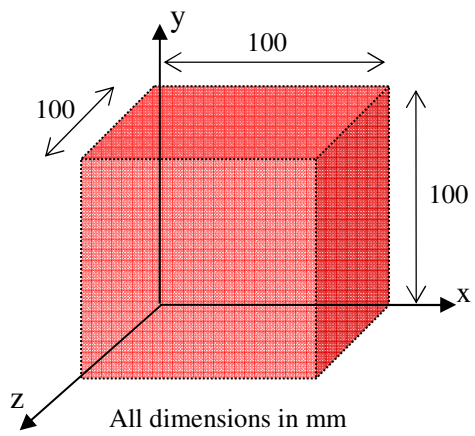

Path 1. Uniaxial tension-compression. Lower surface (y=0) restrained: upper surface (y=100) displaced, firstly in a positive and then a negative direction.

Path 2. Crack formed under normal loading and then shear applied. All sides restrained. Upper surface displaced to 0.05 mm in y direction and then held constant whilst displacement increased in x direction to 0.06mm.

Path 3. Restrained shear. Lower surface restrained whilst upper surface displaced in the x and z directions only with the ratio $u_x/u_z=2/1$.

Figure 3. Example 1 displacement paths.

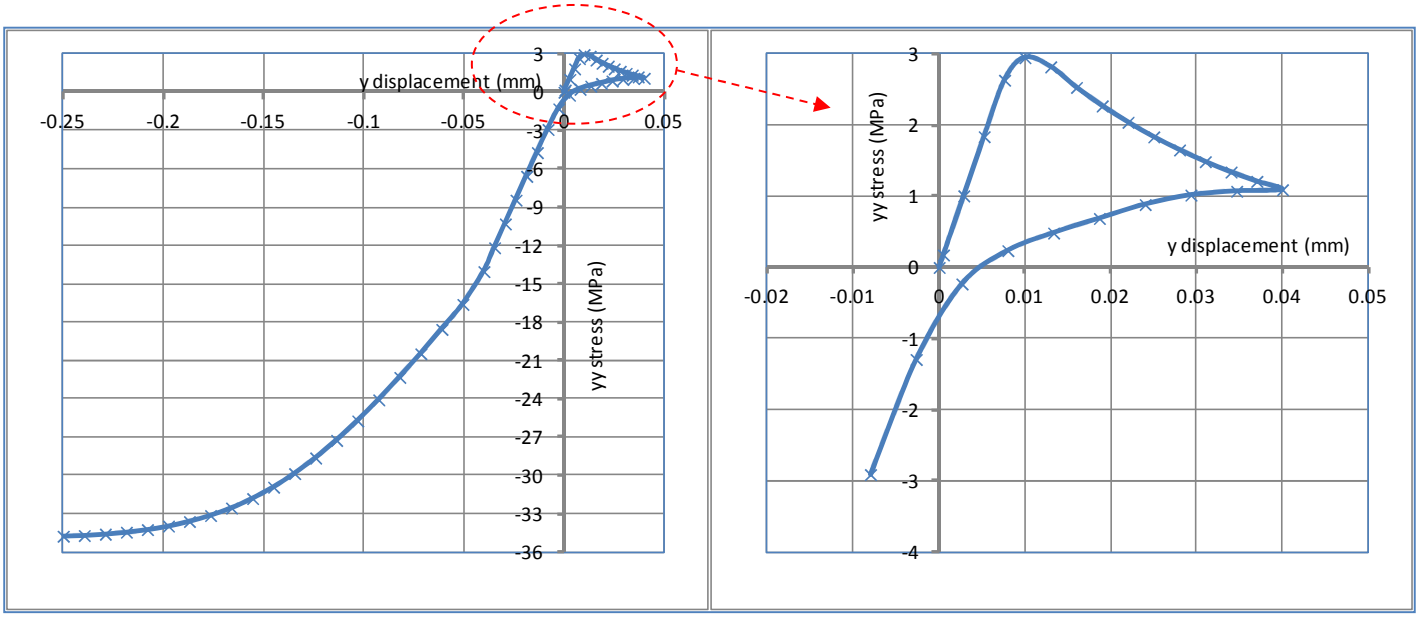

Figure 4. Path 1 responses.

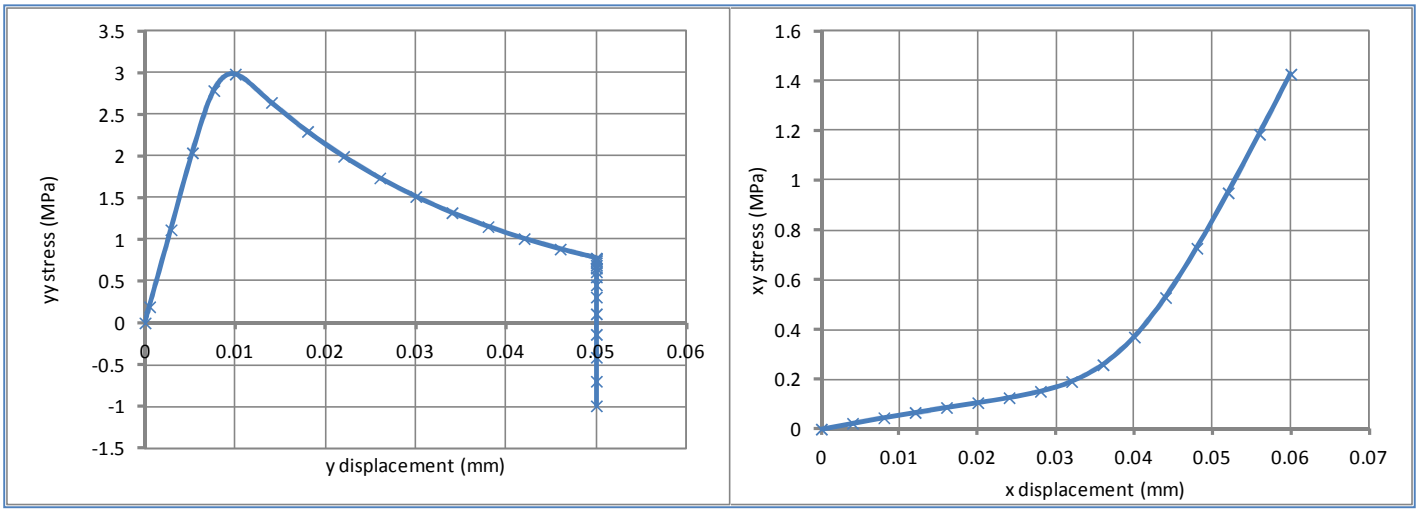

Figure 5. Path 2 responses.

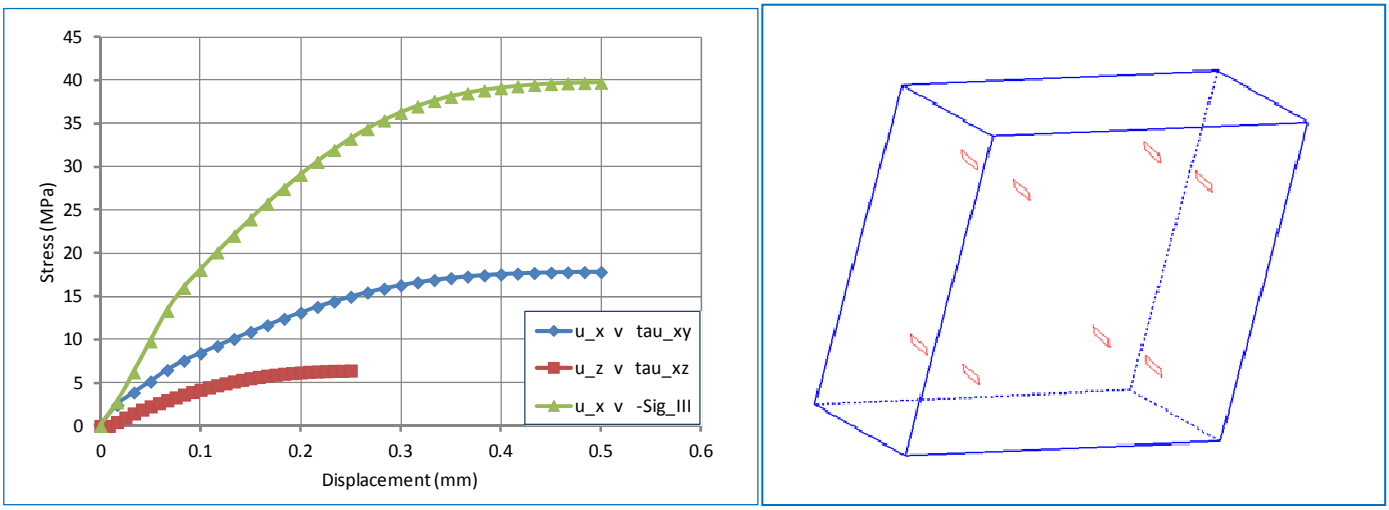

Figure 6. Path 3 response and exaggerated deformed mesh plot showing crack orientations.

Example 2. Direct fracture example

The second example presents results from a number of plane stress analyses of a fracture test specimen. The un-reinforced fracture specimen was tested by Petersson [57] and was loaded in direct tension under displacement control. The dimensions of the specimen are shown in Figure 7, the material properties are given in Table 2 and the three finite element meshes used for the analyses are shown in Figure 8. The analyses are chosen to explore not only the effect of varying the mesh but also the effect of varying the increment size and the SUR option. The number of increments used for the full solutions were either 20 or 50. The analysis using mesh 1 with 20 loading increments was undertaken with the two different SUR options (See Section 2.2). The experimental and numerical load displacement responses from all analyses are shown in Figure 9 in which the average stress is the total vertical load divided by the cross-sectional area at the neck.

The results from all analyses using meshes 1 and 2 are indistinguishable from one another at the scale plotted, with the results from the analyses using SUR1 and SUR2 being coincident to within four decimal places. This result implies that, for this type of problem, the approximation inherent in the SUR2 procedure causes negligible error. The only noticeably different result is that from the distorted mesh but even this, in practical terms, is acceptably close to the other results.

Principal strain plots on exaggerated deformed meshes are given in Figure 10 in order to show the strain localisation bands. The convergence histories of the 20 increment mesh 1 solutions with the two different SUR options are presented in Figure 11. A tighter tolerance was selected than that used for the other examples in order to illustrate the difference in the convergence histories of the two SUR options. The out of balance force norm is plotted for each case for the increment that required the most iterations to achieve convergence. The solutions match up to iteration *itx* (i.e 4), after which the SUR1 solution converges linearly but the SUR2 solution has quadratic convergence.

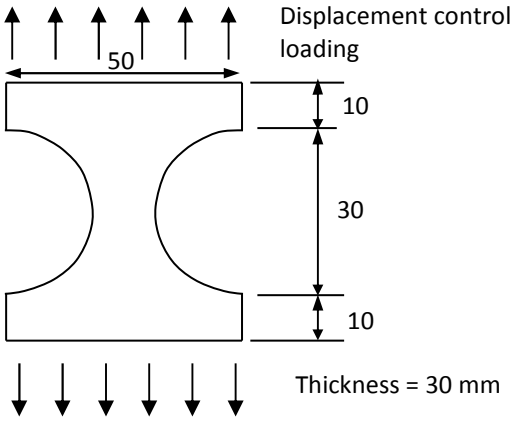

Figure 7. Experimental arrangement.

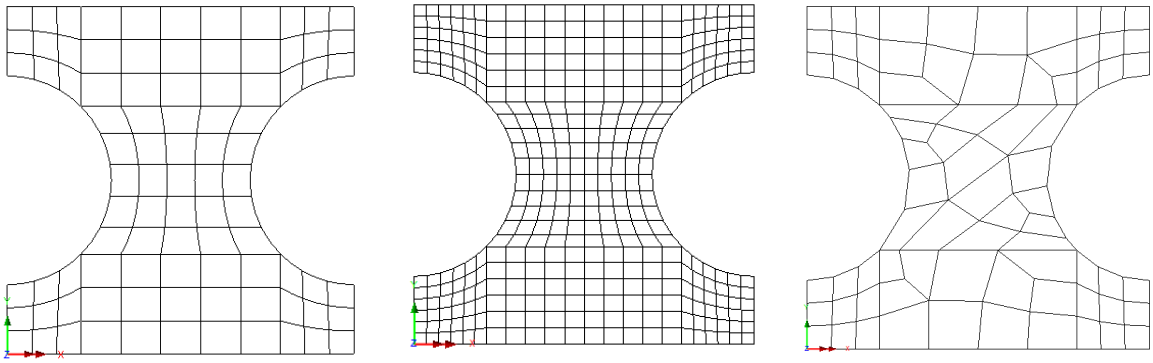

Mesh 1 Mesh 2 Mesh 3

Figure 8. Finite element meshes.

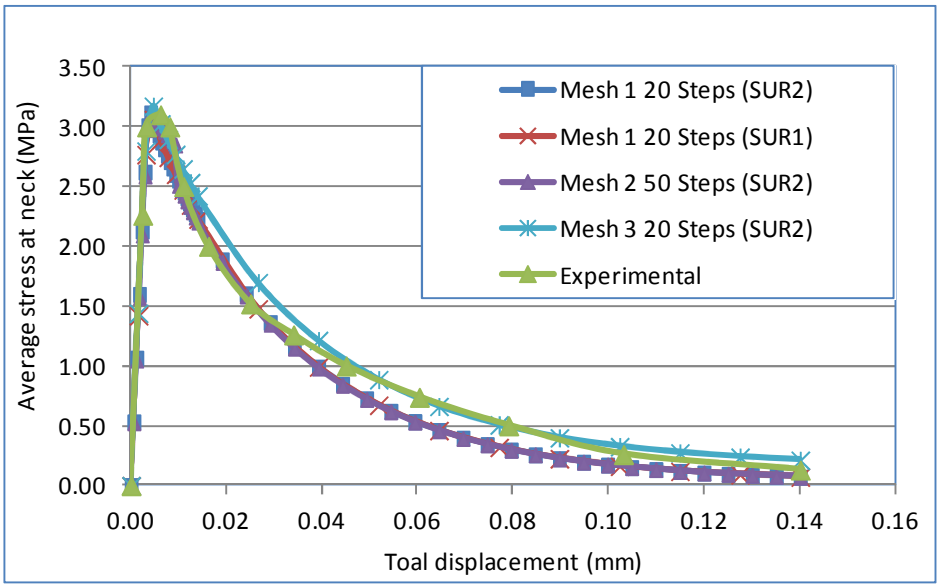

Figure 9. Experimental and numerical load-displacement responses for coarse and fine meshes.

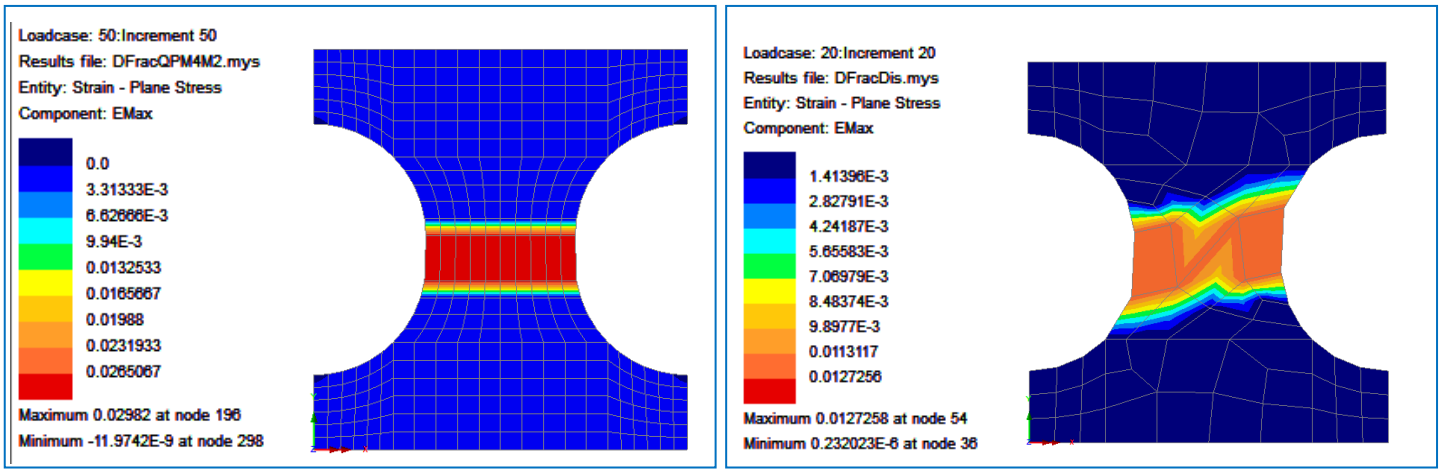

Figure 10. Maximum principal strain plots on deformed meshes for Meshes 2 and 3 at final increment

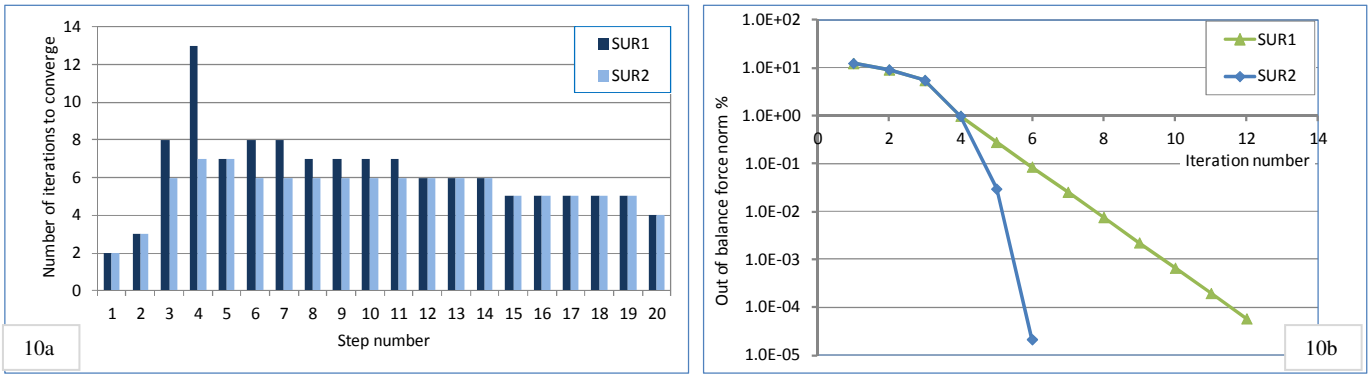

Figure 11. Convergence history: a) Number of iterations to converge: b) ψ_f history for increment 4.

Example 3. Prismatic torsion beam

The third example considers a notched prismatic concrete beam which was originally tested by Brokenshire [58], the full details of which may also be found in Jefferson et al. [59]. As described in the second of the aforementioned references, the beam was previously analysed by the first author but at that time considerable difficulties were encountered in obtaining converged solutions and it was not possible to replicate the load CMOD (crack mouth opening displacement) response. Neither was mesh convergence considered in the original work. We therefore thought that it would be worthwhile to revisit the example and to assess the performance of the new model for this problem.

The experimental arrangement is shown in Figure 12 and the material properties are given in Table 2.

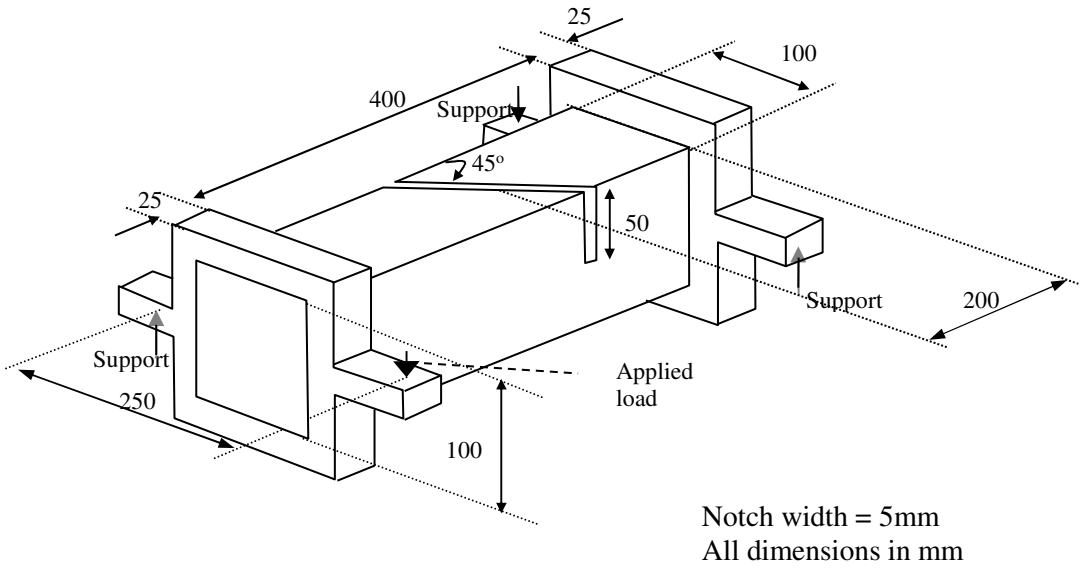

Figure 12. Testing arrangement for notched prismatic torsion test.

The meshes used for the analysis comprised 8-noded hexahedral elements and are shown in Figure 13. The analyses were undertaken with the automatic step selection procedure in which between 50 to 60 steps were used to reach a displacement of 2.5mm at the load position.

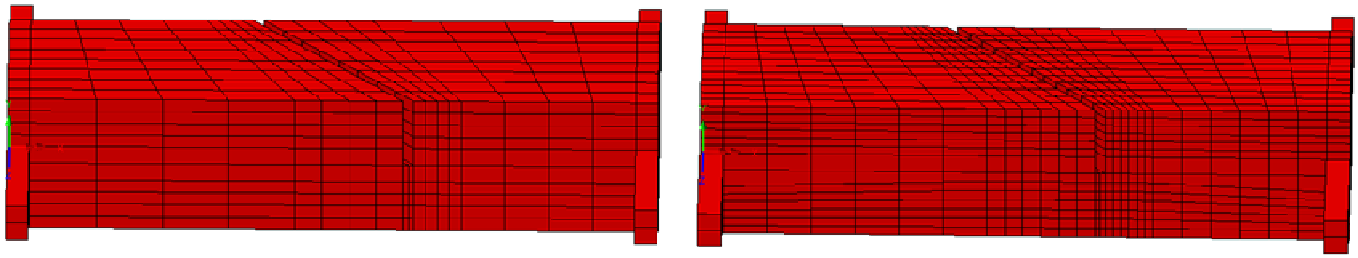

Mesh 1 Mesh 2

Figure 13. Finite element meshes.

The numerical load-CMOD responses, shown in Figure 14, are considerably closer to that of the original experimental study than that achieved with the previous model. The results from the two meshes are almost indistinguishable from each other at the graph scale used. The numerical response tends to a plateau at 0.10kN, rather than 0, which suggests that final failure mode is not quite captured with these meshes and elements. A deformed mesh plot at the final displacement increment for the analysis with mesh 2 is shown in Figure 15. A comparison with the previous analysis [59], which failed to converge after the CMOD reached 0.3mm, shows the benefit of using the SUR approach.

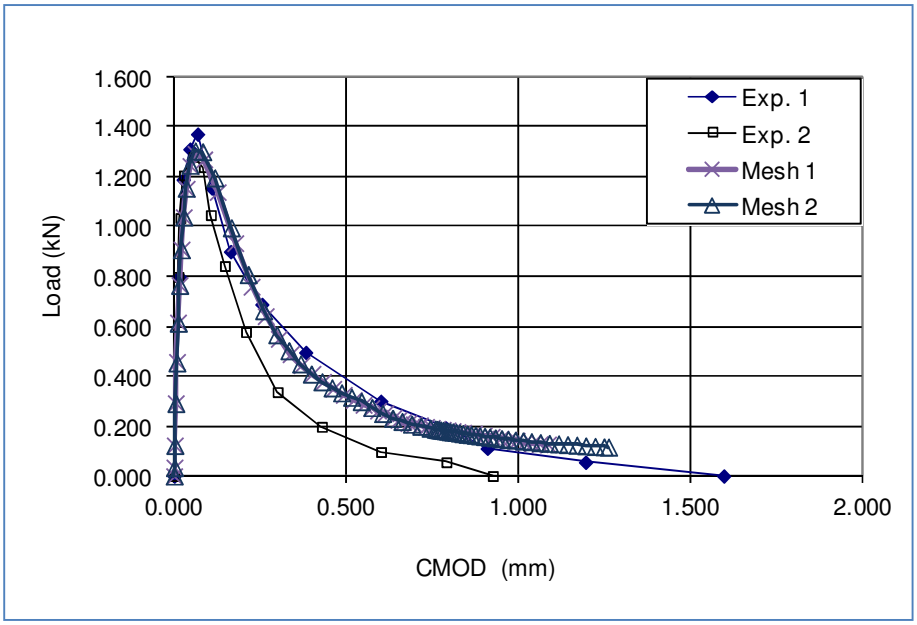

Figure 14. Load CMOD response for Brokenshire's torsion fracture beam.

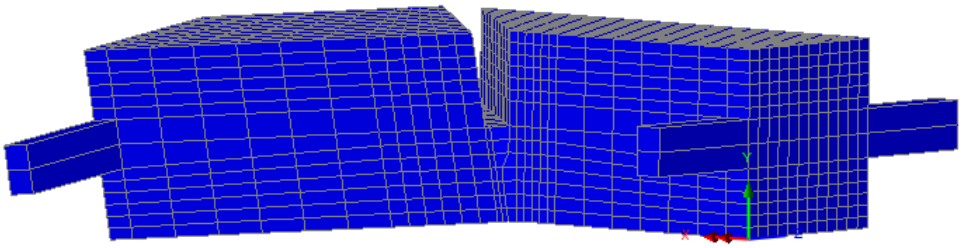

Figure 15. Exaggerated deformed mesh plot at final increment

Example 4. Bresler-Scordelis beam

Example 4 presents a study based on an experimental beam tested long ago by Brelser and Scordleis [60]. The experimental arrangement is shown in Figure 16. The three meshes employed, which make use of symmetry and comprise bilinear elements for concrete and linear 'bar' elements for the reinforcement, are shown in Figures 17 and 18. The load/displacement step parameters used gave solutions in 60 to 100 increments. A graph showing the numerical and experimental load-central deflection (P versus u) curves is given in Figure 19.

The original paper by Bresler and Scordelis gives a 'typical crack pattern' at failure. This showed a diagonal tension shear failure with a dominant shear crack and a horizontal splitting crack just above the level of the main reinforcement. There were also characteristic inclined flexural cracks. The experiment was undertaken under load control and therefore no post-peak load-displacement response data were measured; however, the ability of the model to predict the pre-peak response, failure mode, peak load and stable post-peak response are nevertheless all of interest here. For this purpose, three sets of major principal strain plots are presented in Figure 20 at three different central displacements, the first representing a working load level (at 3mm), the second being just before the peak load (at 6mm) and the third giving the conditions at the final increment. The magnitudes of the strains vary since the softening curve is scaled to maintain constant fracture energy (See section 2.2). Thus, it is the patterns of localised strains which are of interest rather than their absolute magnitudes.

The analyses predict that strain localisation occurs in the working load range, suggesting that the fracture energy approach to computing the strain at the end of the softening curve is appropriate for this RC beam analysis. The analyses captured the inclined flexural cracks, which are at approximately the same average spacing as those given in the original paper, as well as the failure mode. The peak load is predicted well, with the computed peak values being 90%, 98% and 100% of the experimental peak load for meshes 1 to 3 respectively. The immediate post peak response is very close to snap back behaviour but is nevertheless captured by the analyses and the results show clear mesh convergence. The relatively small difference in the predicted post-peak responses from meshes 2 and 3 is considered acceptable in the vicinity of a near brittle collapse.

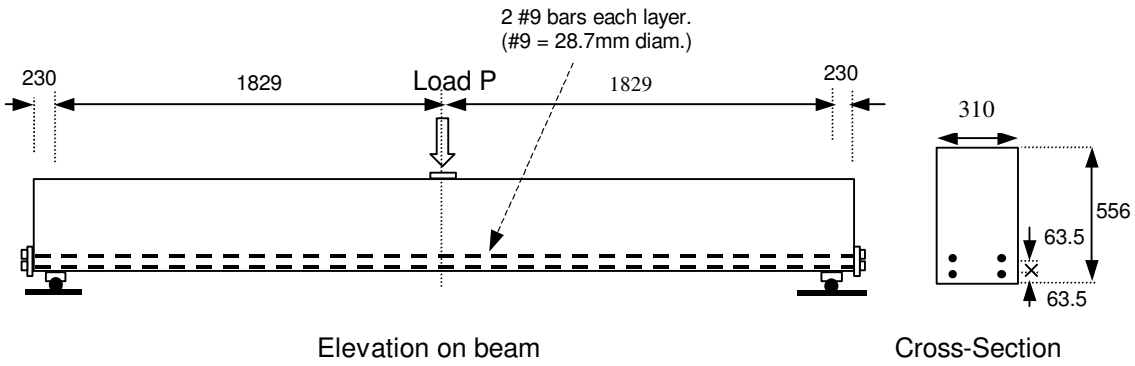

Figure 16. Experimental arrangement.

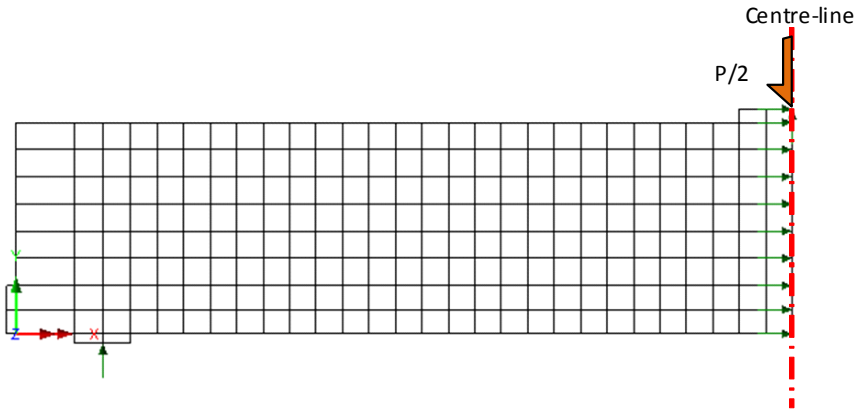

Figure 17. Finite element mesh 1, showing boundary conditions.

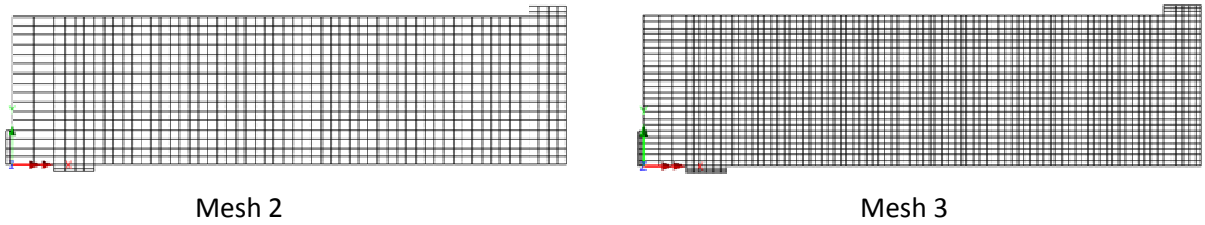

Figure 18. Meshes 2 and 3.

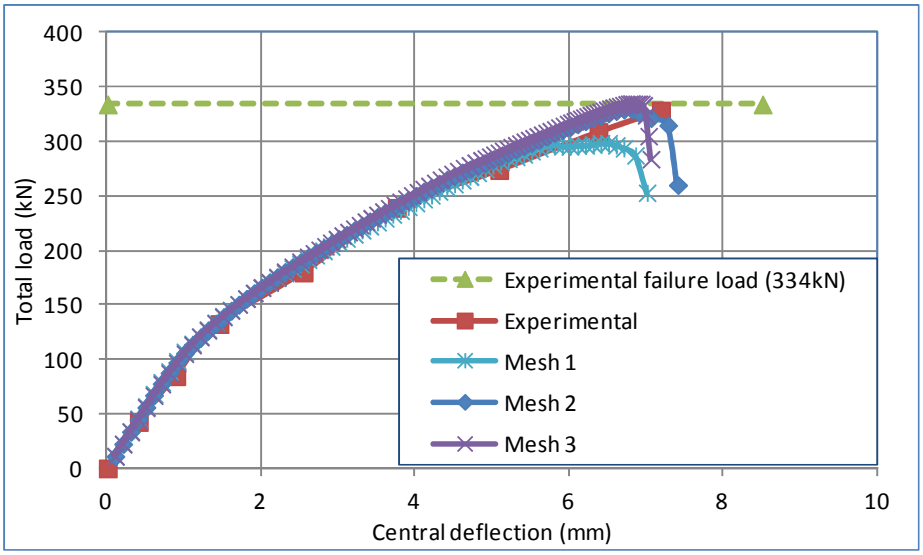

Figure 19. Comparison of load-displacement responses.

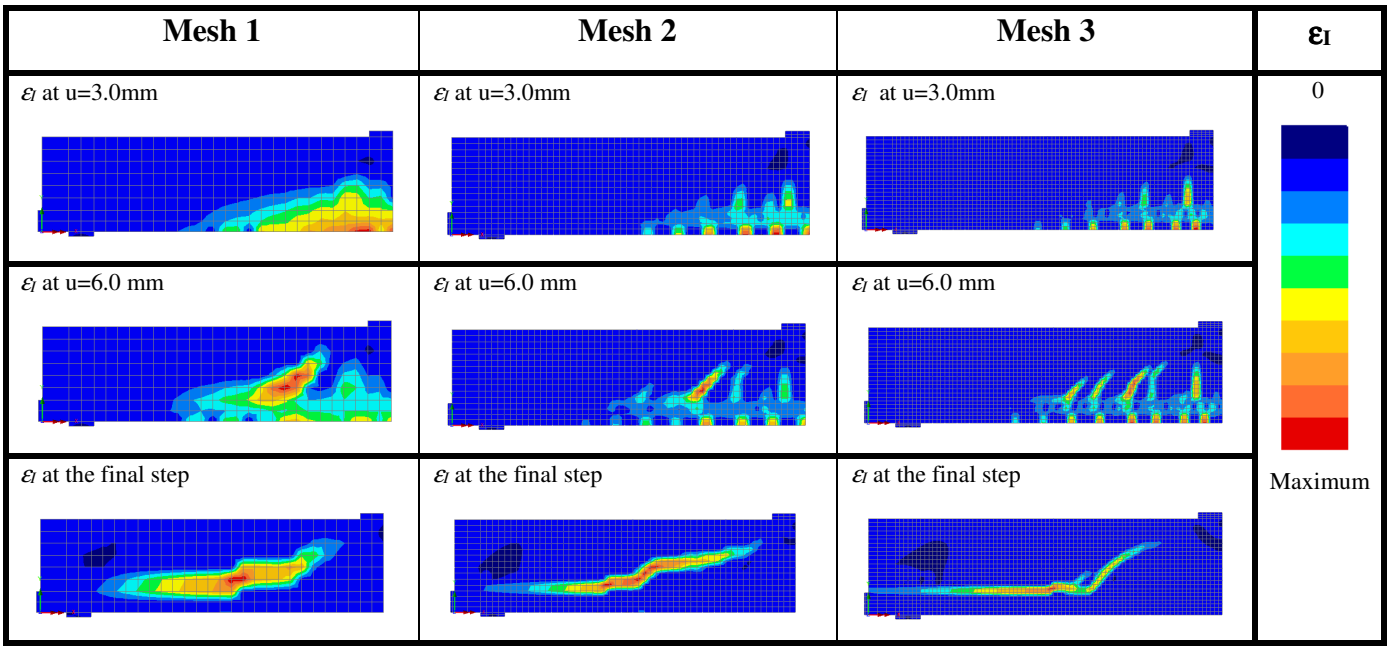

Figure 20. Major principal strain plots showing regions with localised strains.

Example 5. I-Beam test by Kaufmann

The final example considers a test undertaken by Kaufmann [61] on a reinforced concrete I-Beam which was reinforced in both the flange and the web, as shown in Figure 21. The complex loading rig developed for these tests was designed to apply pure shear, with and without axial load, to reinforced concrete members. The particular test considered here (denoted VN2) had zero axial load and was loaded in shear, with a loading unloading cycle to 300kN being applied before final loading to failure. The beam exhibited considerable cracking in shear prior to final failure, which occurred by a shear compression type of failure with some horizontal splitting crack adjacent to the beam flanges.

The beam was analysed using the mesh shown in Figure 22, in which bilinear elements were used for the concrete and linear 'bar' elements for the reinforcement. The material properties are given in Tables 2 and 3.

The mesh includes representation of stiff endplates and the mesh on the left boundary has been extended to allow simulation of the zero rotation restraint with no axial load. Loading on the right hand boundary was by prescribed displacement. The automatic step size selection procedure was used and the solution required 135 increments, including the increments for the loading/unloading cycle. The experimental and numerical load displacement responses are given in Figure 23 and principal strain plots on exaggerated deformed mesh plots at the final load stage are given in Figure 24. The principal strain plot for the continuum elements is used to show the regions of localised strain. A plot of the axial plastic strains in the reinforcement at the final load stage is also provided in Figure 24 in order to show the extent of yielding in the reinforcement.

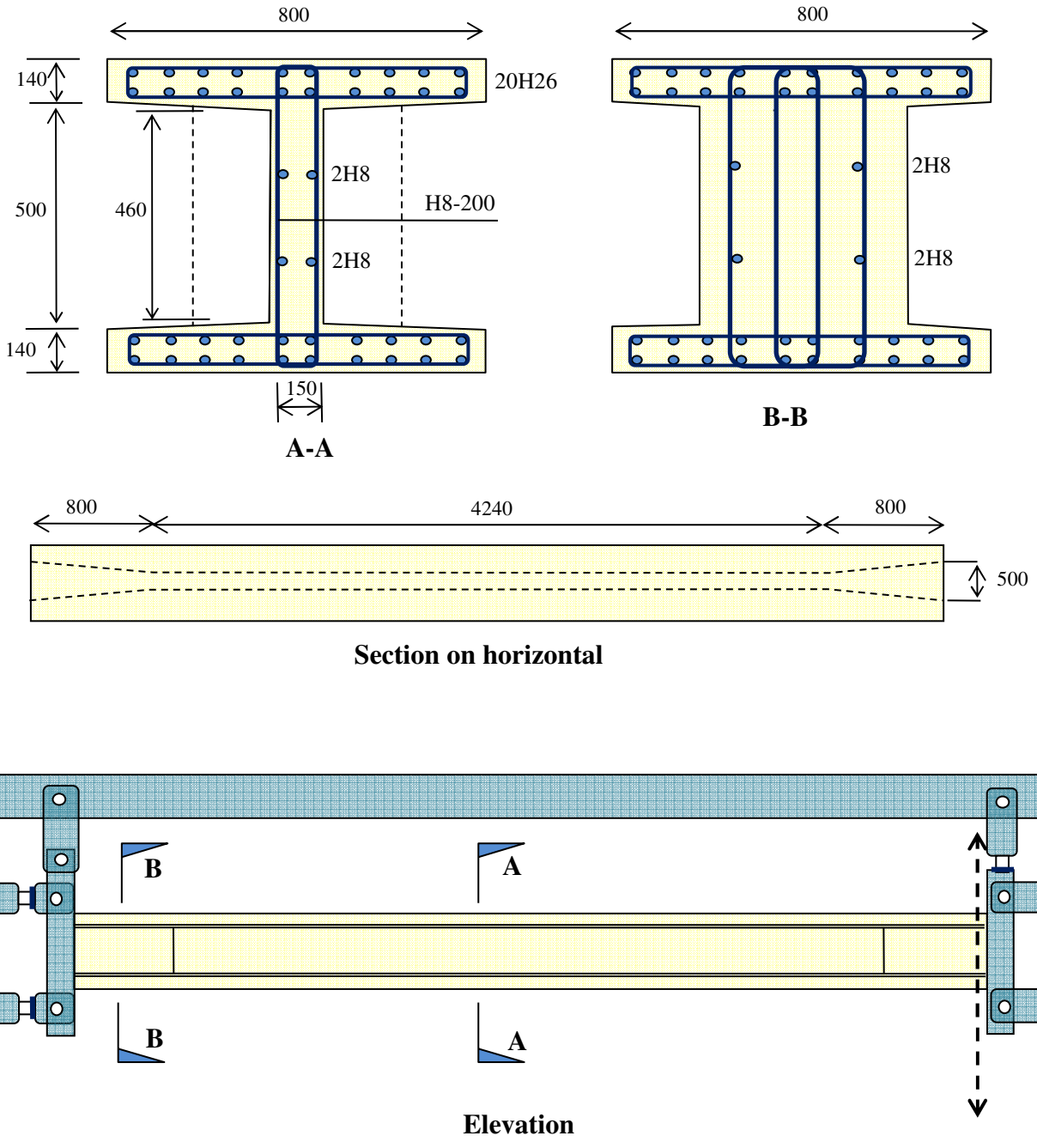

Figure 21. Experimental arrangement for Kaufmann beam.

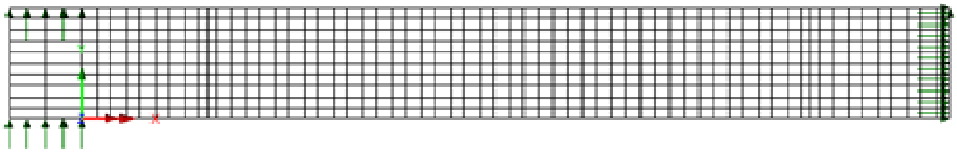

Figure 22. Finite element mesh showing boundary conditions.

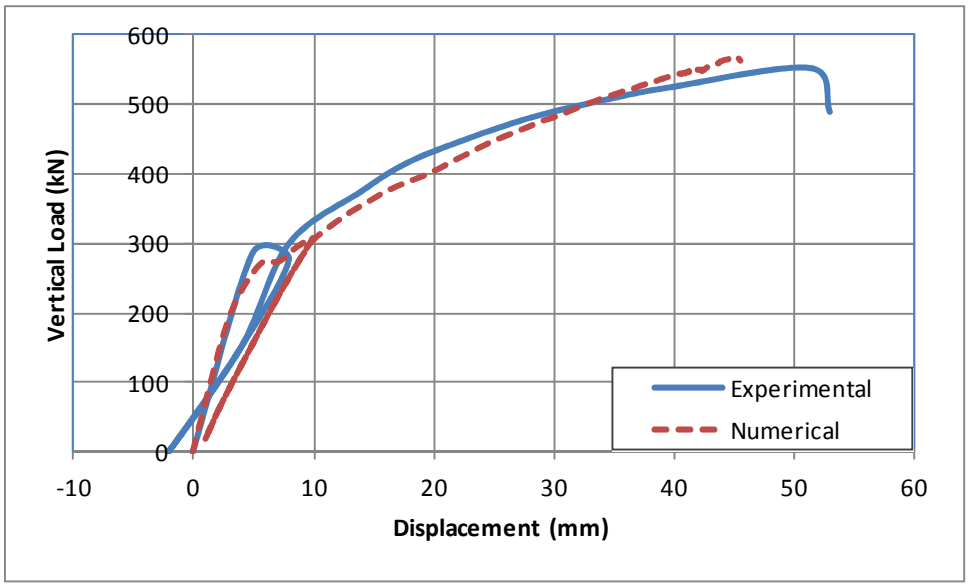

Figure 23. Experimental and numerical responses.

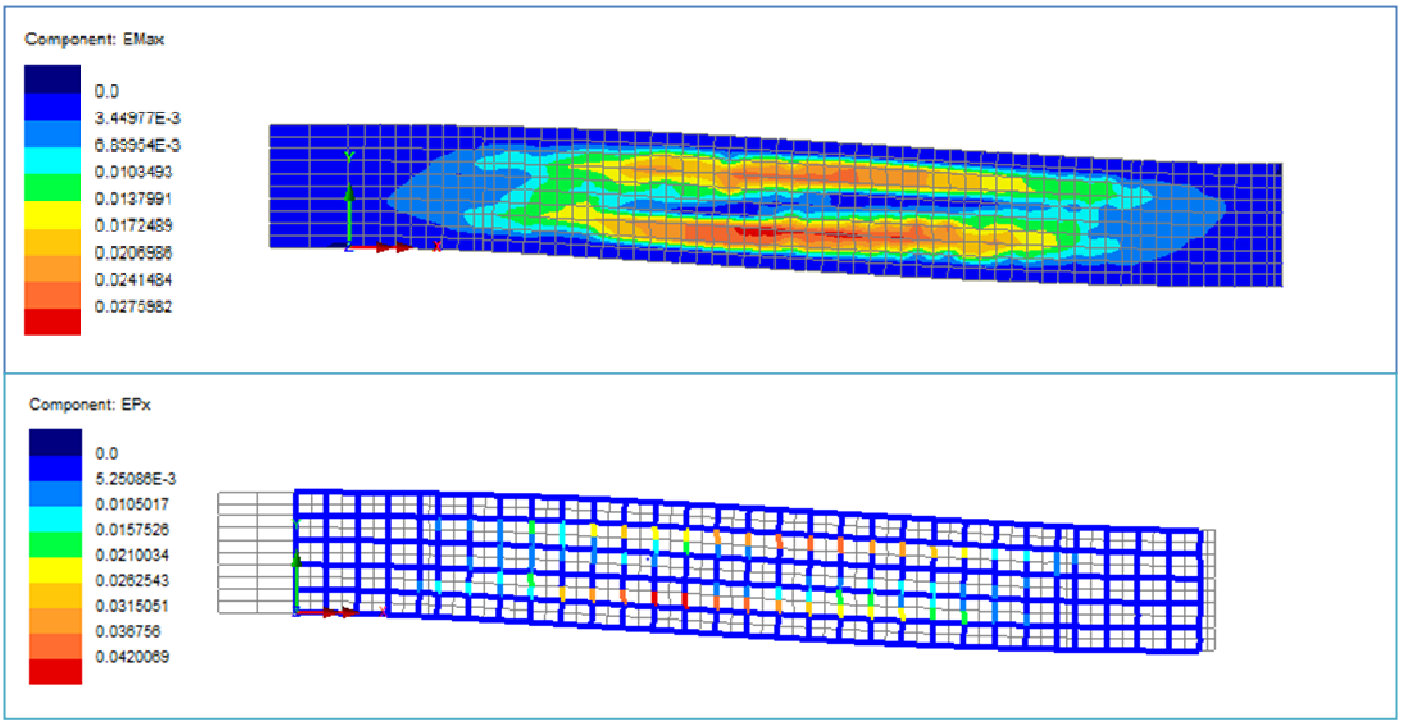

Figure 24. Major principal strain and plastic reinforcement strain plots at final step

A notable feature of the experimental and numerical responses is the jump in displacements at a load of around 300kN. This is little surprising since the shear and flexural reinforcement percentages are both above the code minimum levels required for ductility but it is nevertheless encouraging from the point of view of the model that this jump is captured in the analysis.

The failure mode suggested by the localised strain plot (i.e. assumed crack pattern) is essentially similar to that described for the experiment i.e. diagonal shear cracking and splitting along the web–flange interface. However, in the experiment there was more general diagonal cracking in the flange and horizontal splitting was less dominant than in the analysis. The present analyses included crushing, multi-directional cracking, shear contact (aggregate interlock), reinforcement yield and strain hardening but did not include bond slip or any direct representation of dowel action. Ultimately these factors should be included for a truly comprehensive representation of the beam.

6. CONCLUSIONS

The recently developed smooth unloading-reloading approach for damage mechanics simulations has been combined with a smoothed crack contact sub-model to form a new concrete crack-plane material model. This crack-plane sub-model has then been incorporated into a 3D algorithmic framework, along with a triaxial plasticity model component, to form a new three dimensional finite element material model for concrete. The implementation of the model components using a closest point projection stress recovery algorithm and consistent tangent matrix has resulted in a model that is numerically efficient and computationally robust. The model possesses good convergence properties with respect to a Newton based incremental iterative solution process. It is also shown to be objective with respect to mesh grading and increment size.

The examples show that the new model is able to reproduce the behaviour of a range of plain and reinforced concrete structural elements. In particular, the examples show that the model can realistically predict overall structural responses, crack patterns, post-peak behaviour and failure modes.

REFERENCES

1	ASCE Task Committee on Finite Element Analysis of Reinforced Concrete Structures. Finite element analysis of reinforced concrete structures, 1982, ASCE.
2	Hillerborg M., Modeer M. and Peterson P. Analysis of crack formation and crack growth in concrete by means of fracture mechanics and finite elements. Cement and Concrete Research 1976, 6: 773–782.
3	Bažant Z.P. and Oh B.H. Crack band theory for fracture in concrete. Materials and Structures 1983, 16: 155-177.
4	Pijaudier-Cabot G. and Bažant Z.P. Non-local damage theory, ASCE Journal of Engineering Mechanics 1987, 113: 1512-1533.
5	Jirasek M. and Marfia S. Non-local damage based on displacement averaging. International Journal for Numerical Methods in Engineering 2005, 63 : 77-102.
6	Grassl P. and Jirasek M. Plastic model with non-local damage applied to concrete. International Journal for Numerical and Analytical Methods in Geomechanics 2006, 30 : 71-90.
7	Ru C.Q. and Aifantis E.C. A simple approach to solve boundary-value problems in gradient elasticity. Acta Mechanica 1993, 101: 59-68.
8	Peerlings R.H.J., de Borst R., Brekelmans W.A.M. and de Vree J.H.P. Gradient enhanced damage for quasi-brittle materials", International Journal for Numerical Methods in Engineering 1996, 39(19): 3391 – 3403.
9	de Borst R., Pamin J. and Geers M.G.D. On coupled gradient-dependent plasticity and damage theories with a view to localization analysis. European Journal of Mechanics A :Solids 1999, 18 : 939-962.
10	Rodriguez-Ferran A., Bennett T., Askes H. and Tamayo-Mas E. A general framework for softening regularization based on gradient elasticity. International Journal of Solids and Structures 2011, 48 : 1382-1394.
11	Bennett T. Rodriguez-Ferran A. and Askes H. Damage regularisation with inertia gradients. European Journal of Mechanics A :Solids 2012, 31 : 131-138.
12	Pijaudier-Cabot G, Grégoire D (2014). A review of non-local continuum damage: modelling of failure? Networks and heterogeneous media 9(4), 575-597
13	Dubé J.F., Pijaudier-Cabot G. and La Borderie C. Rate dependent damage model for concrete in dynamics. ASCE Journal of Engineering Mechanics 1996, 122 : 939-947.
14	Wang W. M., Sluys L. J. and de Borst R. Viscoplasticity for instabilities due to strain softening and strain-rate softening. International Journal for Numerical Methods in Engineering 1997, 40: 3839–3864.
15	Belytschko T. and Black T. Elastic crack growth in finite elements with minimal remeshing. International Journal for Numerical Methods in Engineering 1999, 45 : 601-620.
16	Moës N., Dolbow J. and Belytschko T. A finite element method for crack growth without remeshing. International Journal for Numerical Methods in Engineering 1999, 46:131-150.
17	Fries T.P. and Belytschko T. The extended/generalized finite element method: An overview of the method and its applications. International Journal for Numerical Methods in Engineering 2010, 84 : 253-304.
18	Kaczmarczyk, L., Pearce, C.J., Bicanic, N., and de Souza Neto, E. Numerical multiscale solution strategy for fracturing heterogeneous.Computer Methods in Applied Mechanics and Engineering 2010, 199 :1100-1113.
19	Nguyen V.P., Stroeven M. and Sluys L.J. Multiscale failure modelling of concrete: micromechanical modelling, discontinuous homogenization and parallel computations. Computer Methods in Applied Mechanics and Engineering 2012, 201-204: 139-156.
20	Oliver J., Husepe A.E., Pulido M.D.G. and Chaves E. From continuum mechanics to fracture mechanics: The strong discontinuity approach. Engineering Fracture Mechanics 2001, 69: 113-136.
21	Oliver J., Husepe A.E. and Samaniego E. A study on finite elements for capturing strong discontinuities. International Journal for Numerical Methods in Engineering 2003, 56 :2135-2161.
22	Linder C. and Armero F. Finite elements with embedded strong discontinuities for the modeling of failure in solids. International Journal for Numerical Methods in Engineering 2007, 72 :1391-1433.

23	Dias-da-Costa D., Alfaiate J., Sluys L. J. and Júlio E. A comparative study on the modelling of discontinuous fracture by means of enriched nodal and element techniques and interface elements. International Journal of Fracture 2010, 161 : 97–119.
24	Dias-da-Costa D., Alfaiate J., Sluys L.J, Areias P. and Julio E. An embedded formulation with conforming finite elements to capture strong discontinuities. International Journal for Numerical Methods in Engineering 2013, 93 : 224–244.
25	Zhang Y, Lackner R, Zeiml M,, Mang H A (2015). Strong discontinuity embedded approach with standard SOS formulation: Element formulation, energy-based crack-tracking strategy, and validations. Comput. Methods Appl. Mech. Engrg. 287, 335-366
26	Cervera M. Chiumenti M. and Codina R. Mesh objective modelling of cracks using continuous linear strain and displacement interpolations. International Journal for Numerical Methods in Engineering 2011, 87 : 962-987.
27	Mazars J. A description of micro and macro scale damange of concrete structures. Engineering Fracture Mechanics 1989, 25 : 729-737.
28	Mazars J. and Pijaudier-Cabot G. Continuum damage theory - application to concrete. Journal of Engineering Mechanics 1989, 115 : 345-365.
29	Feenstra P.H. and de Borst R. A plasticity model and algorithm for mode-I cracking in concrete. International Journal for Numerical Methods in Engineering 1995, 38 : 2509-2529.
30	Etse G. and Willam K. Fracture energy formulation for inelastic behavior of plain concrete. Journal of Engineering Mechanics 1994, 120 : 1983-2011.
31	Lubliner J., Oliver J., Oller S. and Oñate E. Continuum damage theory - application to concrete. International Journal of Solids and Structures 1989, 25 : 299-326.
32	Crisfield M.A. Non-linear Finite Element Analysis of Solids and Structures Vol.1. John Wiley & Sons, Chichester, UK, 1991.
33	de Borst R, Crisfield MA, Remmers JJC, Verhoosel CV. Non-linear finite element analysis of solids and structures.
34	Oliver J., Husepe A.E., Blanco S. and Linero D.L. Stability and robustness issues in numerical modelling of material failure with the strong discontinuity approach. Computer Methods in Applied Mechanics and Engineering 2006, 195 : 7093-7114.
35	Oliver J., Huespe AE and Cante JC. An implicit/explicit integration scheme to increase computability of non-linear material and contact/friction problems, Computer Methods in Applied Mechanics and Engineering 2008, 197: 1865–1889.
36	Rots J.G., Belletti B. and Invernizzi S. Robust modeling of RC structures with an 'event-by-event' strategy. Engineering Fracture Mechanics 2008, 75(3–4): 590–614.
37	Graca-e-Costa R., Alfaiate J., Dias-da-Costa D. and Sluys L.J. A non-iterative approach for the modelling of quasi-brittle materials . International Journal of Fracture 2012, 178 : 281-298.
38	Slobbe A T, Hendriks MAN , Rots JG . Smoothing the propagation of smeared cracks. Engineering Fracture Mechanics 132 (2014) 147–168
39	Rots J, de Borst R. Analysis of mixed mode fracture in concrete. ASCE Journal of Engineering Mechanics 1987; 113(11):1739–1758.
40	ACI-ASCE Committee 426. The shear strength of reinforced concrete members. Journal of the Structural Division 1973; 99(6).
41	Jefferson AD, Mihai IC, The simulation of crack opening-closing and aggregate interlock behaviour in finite element concrete models, International Journal for Numerical Methods in Engineering ISSN 0029-5981 10.1002/nme.4934. (2015)
42	Reinhardt H.W. 1984. Fracture mechanics of an elastic softening material like concrete. Heron, 29(2), Delft, The Netherlands, 1-42. 1988.

43	Sellier A., Casaux-Ginestet G. Buffo-Lacarrière L. and Bourbon X. Orthotropic damage coupled with localised crack reclosure processing. Part I: Constitutive laws. Engineering Fracture Mechanics 2013, 978:148-167.
44	Alnaas W, Jefferson AD, A smooth unloading-reloading approach for the nonlinear finite element analysis of quasi-brittle materials, Engineering Fracture Mechanics , (2015) ISSN 0013-7944 10.1016/j.engfracmech.2015.04.018
45	Jefferson AD. Craft - a plastic-damage-contact model for concrete. I. Model theory and thermodynamic considerations, International Journal of Solids and Structures 2003, 40(22): 5973-5999.
46	Jefferson AD. Craft - a plastic-damage-contact model for concrete. II. Model implementation with implicit return-mapping algorithm and consistent tangent matrix, International Journal of Solids and Structures 2003, 40(22): 6001-6022.
47	Walraven J.C. and Reinhardt H.W. Theory and experiments on the mechanical behavior of cracks in plain and reinforced concrete subjected to shear loading. Heron 26(1A), Delft, The Netherlands. 1981.
48	Jacobsen JS, Poulsen PN, Olesen JF. Characterization of mixed mode crack opening in concrete. Materials and Structures 2012; 45:107–122.
49	Paulay T, Loeber PJ. Shear transfer by aggregate interlock. In *Shear in Reinforced Concrete*, Publication SP-42, American Concrete Institute 1974, 1-15.
50	Jefferson A.D. A constitutive model for aggregate interlock on formed crack planes. International Journal of Numerical and Analytical Methods in Geomechanics 2002, 26: 1-21.
51	Reinhardt HW. Fracture mechanics of an elastic softening material like concrete. Heron 1984; 2:1–42.
52	Simo JC and Hughes TJR. Computational Inelasticity. (1998)
53	Muralidhara S, Raghu Prasad BK, Karihaloo BL, Singh RK. Size-independent fracture energy in plain concrete beams using tri-linear model. Construction and Building Materials 25 (2011) 3051–3058
54	van Mier, J.G.M., 1997. Fracture processes of concrete, CRC Press.
55	Kotsovos, M.D., Newman, J B., 1979. A mathematical description of the deformable behavior of concrete under complex loading. Magazine of concrete research. 31, 77-90.
56	Jirasek M, Grassl P. Evaluation of directional mesh bias in concrete fracture simulations using continuum damage models. Engineering Fracture Mechanics 2008, 75, 1921–1943
57	Petersson P. Crack growth and development of failure zones in plain concrete and similar materials. Lund Institute of Technology, Sweden. 1981
58	Brokenshire D.R. A study of torsion fracture tests, PhD Thesis, Cardiff University, U.K. 1996.
59	Jefferson A.D., Barr B.I.G., Bennett T., Hee S.C. Three dimensional finite element simulations of fracture tests using the craft concrete model, *Computers and Concrete* 2004, **1**(3): 261-284.
60	Bresler B. and Scordelis A.C. Shear strength of reinforced concrete beams. Journal of the American Concrete Institute, January, 1963, 51-72
61	Kaufmann W. Strength and Deformations of Structural Concrete Subjected to In-Plane Shear and Normal Forces. PhD Thesis, Swiss Federal Institute of Technology Zurich. 1998.
62	LUSAS v15. www.LUSAS.com (2015)

Acknowledgements

We gratefully acknowledge support from the INNOVATEUK KTP 8380. We would also like to acknowledge Mr Gian Nick for his feedback on using concrete models on real engineering problems and for suggesting the benchmark test of Kaufmann.

APPENDIX A. Summary of triaxial plasticity model

The yield function, plastic potential and hardening functions for the plasticity component of the present model are all taken from Reference [45] and summarised in this Appendix.

The yield function is given by

$$F(\boldsymbol{\sigma}, Z(\kappa)) = \sqrt{J_2}\cdot A_r(\theta) + \left(\alpha + \frac{\gamma}{3}\right)\cdot I_1 \cdot Z - f_c \cdot Z \cdot (1-\alpha) \tag{A1}$$

where $A_r(\theta) = \rho_c \left(\dfrac{2\cos(\theta)^2 + b^2}{\cos(\theta) + b\sqrt{2\cos(\theta)^2 + c}} \right)$

and I_1 = 1st stress invariant, J_2 = 2nd deviatoric stress invariant, θ is the Lode angle (with range 0 to 60°) and Z is a friction hardening factor, which is a function of the work hardening parameter κ: Z varies from Z_0 to 1. Z_0 is a material parameter which in all the examples in this paper is set to 0.6. The biaxial to uniaxial compressive strength ratio b_r (typically = 1.15) is a material parameter and is used in the computation of the other parameters in equation (A1), as follows;

$$\alpha = \frac{b_r - 1}{2b_r - 1}, \quad b = \sqrt{2} - 1, \quad c = \frac{5}{2} - 2\sqrt{2}, \quad \rho = 1/\sqrt{2}, \quad \gamma = \frac{3(1-\rho)}{2\rho - 1}, \quad \rho_c = \sqrt{3} + \frac{\gamma}{\sqrt{3}}$$

The plastic potential function is given by;

$$G(\boldsymbol{\sigma}, Z(\kappa)) = \sqrt{J_2}\, A_r(\theta) + \left(\alpha + \frac{\gamma}{3}\right) I_1\, Z\, \psi - f_c\, Z\, \psi\, (1-\alpha) \tag{A2}$$

This has the same form as the yield function with the exception of the addition of the dilatancy term, ψ. ψ is a material parameter which normally set to -0.1.

The flow rule is derived from the plastic potential in the standard way as follows

$$\dot{\boldsymbol{\varepsilon}}_p = \frac{\partial G}{\partial \boldsymbol{\sigma}} \dot{\lambda}_{pl} \tag{A3}$$

λ_{pl} is the plastic multiplier, which obeys the condition $\dot{\lambda}_{pl} \geq 0$ and $\dot{\boldsymbol{\varepsilon}}_{\mathrm{p}}$ is the plastic strain rate.

The work hardening parameter, expressed in rate form, is given by

$$\dot{\kappa} = \mathrm{X}(\boldsymbol{\sigma})\boldsymbol{\sigma}^{\mathrm{T}}\dot{\boldsymbol{\varepsilon}}_{\mathrm{p}} \tag{A4}$$

in which $X(\boldsymbol{\sigma})$ is ductility parameter which depends upon the first stress invariant as follows

$$X = e^{\chi} + e^{\chi - 1} + X_I$$
$$where \quad \chi = \frac{I_1}{f_c * 0.9} + 0.55 \quad and \quad X_I = 0.0022 \tag{A5}$$

The basic friction hardening/softening function for Z gives a smooth transition from pre to post peak behaviour, as follows;

$$Z = Z_0 + \frac{(1 - Z_0)}{a_c}\, e^{-c\eta} \left(1 - e^{-c\eta}\right) \tag{A6}$$

where $\eta_c = \kappa / \kappa_p$; κ_p = value of κ at the peak yield surface position and is given by $\kappa_p = f_c\left(0.72\varepsilon_c - \frac{f_c}{2E}\right)$.

On order to ensure that the peak occurs at Z = 1, the constants must satisfy the following relationships

$$c_{c1} = \frac{c_{c2}\, e^{-c}}{1 - e^{-c}} \qquad \text{and} \qquad a_c = e^{-c}\left(1 - e^{-c}\right).$$

The actual values used are c_{c2}= 5, c_{c1} = 0.0339182745 and a_c = 0.9601372615